2014

Optimal Basis For Ultrasound Rf Apertures: Applications to Real-Time Compression and Beamforming

Sharmin Kibria
University of Massachusetts Amherst

OPTIMAL BASIS FOR ULTRASOUND RF APERTURES: APPLICATIONS TO REAL-TIME COMPRESSION AND BEAMFORMING

A Thesis Presented

by

SHARMIN KIBRIA

Submitted to the Graduate School of the
University of Massachusetts Amherst in partial fulfillment
of the requirements for the degree of

MASTER OF SCIENCE IN ELECTRICAL AND COMPUTER ENGINEERING

February 2014

Electrical and Computer Engineering

OPTIMAL BASIS FOR ULTRASOUND RF APERTURES: APPLICATIONS TO REAL-TIME COMPRESSION AND BEAMFORMING

A Thesis Presented

by

SHARMIN KIBRIA

Approved as to style and content by:

Patrick A. Kelly, Chair

Dev Gupta, Member

Marco F. Duarte, Member

C. V. Hollot, Department Chair
Electrical and Computer Engineering

ACKNOWLEDGEMENTS

Thanks to my thesis committee members-my advisor and chair of the committee Prof. Patrick A. Kelly and committee members Prof. Dev Gupta, Prof. Marco F. Duarte for their guidance and help. Not to mention Jai Gupta and the late Linda Gupta for their kind contributions in the research as well.

ABSTRACT

OPTIMAL BASIS FOR ULTRASOUND RF APERTURES: APPLICATIONS TO REAL-TIME COMPRESSION AND BEAMFORMING

FEBRUARY 2014

SHARMIN KIBRIA

B.Sc., BANGLADESH UNIVERSITY OF ENGINEERING AND TECHNOLOGY

M.S.E.C.E., UNIVERSITY OF MASSACHUSETTS AMHERST

Directed by: Professor Patrick A. Kelly

Modern medical ultrasound machines produce enormous amounts of data, as much as several gigabytes/sec in some systems. The challenges of generating, storing, processing and reproducing such voluminous data has motivated researchers to search for a feasible compression scheme for the received ultrasound radio frequency (RF) signals. Most of this work has concentrated on the digitized data available after sampling and A/D conversion. We are interested in the possibility of compression implemented directly on the received analog RF signals; hence, we focus on compression of the set of signals in a single receive aperture. We first investigate the model-free approaches to compression that have been proposed by previous researchers that involve applications of some of the well-known signal processing tools like Principal Component Analysis (PCA), wavelets, Fourier Transform, etc. We also consider Bandpass Prolate Spheroidal Functions (BPSFs) in this study. Then we consider the derivation of the optimal basis for the RF signals assuming a white noise

model for spatial inhomogeneity field in tissue. We first derive an expression for the (time and space) autocorrelation function of the set of signals received in a linear aperture. This is then used to find the autocorrelation's eigenfunctions, which form an optimal basis for minimum mean-square error compression of the aperture signal set. We show that computation of the coefficients of the signal set with respect to the basis is approximated by calculation of real and imaginary part of the Fourier Series coefficients for the received signal at each aperture element, with frequencies slightly scaled by aperture position, followed by linear combinations of corresponding frequency components across the aperture. The combination weights at each frequency are determined by the eigenvectors of a matrix whose entries are averaged cross-spectral coefficients of the received signal set at that frequency. The principal eigenvector generates a combination that corresponds to a variation on the standard delay-and-sum beamformed aperture center line, while the combinations from other eigenvectors represent aperture information that is not contained in the beamformed line. We then consider how to use the autocorrelation's eigenfunctions and eigenvalues to generate a linear minimum mean-square error beamformer for the center line of each aperture. Finally, we compare the performances of the optimal compression basis and to that of the 2D Fourier Transform.

TABLE OF CONTENTS

LIST OF TABLES

Table **Page**

LIST OF FIGURES

Figure **Page**

CHAPTER 1

MEDICAL ULTRASOUND: IMAGE FORMATION AND COMPRESSION PROBLEM

1.1 Introduction

Ultrasound, one of the most popular modalities in medical imaging, is used to image internal organs of the human body, map blood flow and show tissue motion. Its popularity arises from its high resolution real-time image generation capability without the use of harmful radiation and mostly non-invasive nature of application. An ultrasound system generates images by sending high frequency sound waves inside the body and then processing the received returns reflected from the organs. This chapter gives a general idea about how ultrasound images are generated, the challenges of processing the signals and the motivation behind our work with ultrasound RF signals.

1.2 General Idea Behind Ultrasound Imaging

The central element of an ultrasound system is the array of piezoelectric ultrasound transducers. Transducers are devices that convert one form of energy into another by changing their internal structure. Ultrasound transducers convert electrical energy into acoustical energy and vice versa. A short but high frequency electrical pulse in the 2MHz to 20MHz range is used to excite the transducers in the ultrasound transmitter to generate the sound waves. The transmitted waves get reflected by the internal organs and are received by the receiving transducer array. The transducers in the receiver convert the received sound waves into electrical signals.

To image an organ, the portion of interest is at first divided into several scan lines. Then a number of transducer elements in the transmitter array (also called an aperture for that scan line) are excited using a high voltage and short electrical pulse. The sound wave generated in each transducer is then delayed appropriately to focus onto a specific point on a specific scan line. This process is called transmit beamforming. The focused sound wave then propagates along the scan line and gets reflected as it goes through various tissue layers with different material properties. The reflected sound waves are received at the receiver transducer array and are converted into electrical signals. The signals received at different elements of the array are aligned by again applying appropriate delays and then summed to get the received beamformed signal. Then an image line is generated by detecting peaks in the beamformed signal using envelope detection and then log compression is used to reduce the dynamic range for efficient display. Once all the amplitudes for all the scan lines have been detected, scan conversion needs to be performed to display the image on a CRT monitor for analysis by the doctor or ultrasound technician.

1.3 The Challenges in Ultrasound Signal Processing and the Motivation for Our Work

Although ultrasound has the advantage of not using harmful radiation, the image quality is far behind that of other imaging modalities. To scan large areas quickly and to improve the image quality, the number of transducer elements in the transmitter and receiver array and the sampling frequency needs to be increased. In modern ultrasound systems, a typical transducer array can have 64-256 elements and the number is expected to grow rapidly in the future. The increasing number of transducer elements complicates the front end of the system. As these transducers can operate at a sampling frequency of 25-60 MHz, they can even generate tens of Gigabytes or tens of billions of samples per second for high-resolution images. Processing,

storage, transportation and reproduction of the huge number of samples can be quite expensive.

From an ultrasound system designer's point of view, the challenges are to reduce the cost of processing by finding a feasible compression scheme that reduces the number of samples needed to process, retains the quality of the image, and simplifies the front end of the ultrasound system. Most of the compression schemes have been implemented digitally and require analog-to-digital conversion before processing, which is quite expensive. These signal processing challenges motivated us to formulate a cost effective real-time compression scheme. As beamforming of received pulse-echo data generally involves the combination of signals from multiple channels within an aperture, we also develop a scheme for minimum mean-square error (MSE) beamforming that is compatible with our compression scheme.

1.4 Our Contributions and Organization of Rest of the Thesis

In our work we are interested in the possibility of compression of the set of signals in a single receive aperture. We first investigate the model-free approaches to compression that have been proposed by previous researchers that involve applications of some of the well-known signal processing tools like Principal Component Analysis (PCA), Wavelets, Fourier Transform, etc. We also consider Bandpass Prolate Spheroidal Functions (BPSFs) in this study.

Then we consider the derivation of the optimal basis for the RF signals assuming a white noise model for spatial inhomogeneity field in the tissue. We first derive an expression for the (time and space) autocorrelation's eigenfunctions, which form an optimal basis for compression of the aperture signal set. We show that computation of the coefficients of the signal set with respect to the basis is approximated by calculation of the Fourier Series coefficients for the received signal at each aperture

element, with frequencies scaled by aperture position, followed by linear combinations of corresponding frequency components across the aperture. The combination weights at each frequency are determined by the eigenvectors of a matrix whose entries are averaged cross-spectral coefficients of the received signal set at that frequency. The principal eigenvector generates a combination that corresponds to a variation on the standard delay-and-sum beamformed aperture center line, while the combinations from other eigenvectors represent aperture information that is not contained in the beamformed line. We then consider how to use the autocorrelation's eigenfunctions and eigenvalues to generate a linear minimum mean-square error (LMMSE) beamformer for the center line of each aperture. Finally, we compare the compression performances of the optimal basis and 2D Fourier Transform.

Chapter 2 provides a simple description of the functionality of the portion of the ultrasound system we are interested in the analog front-end and beamformer. In chapter 3, we discuss some significant previous works on ultrasound RF compression and also investigate the performance of some of those techniques. In chapter 4, we discuss how we developed the optimal basis approach, its compression performance, and the minimum MSE beamformer. We also compare the compression performances of optimal basis and 2D Fourier Transform. This chapter is followed by concluding remarks and suggestions for future work.

CHAPTER 2

ULTRASOUND ANALOG FRONT-END AND BEAMFORMER AT A GLANCE

This chapter provides a brief description of the functionality of the analog front-end and beamforming part of the ultrasound system. This will make it easier to understand which part of the overall system we are dealing with.

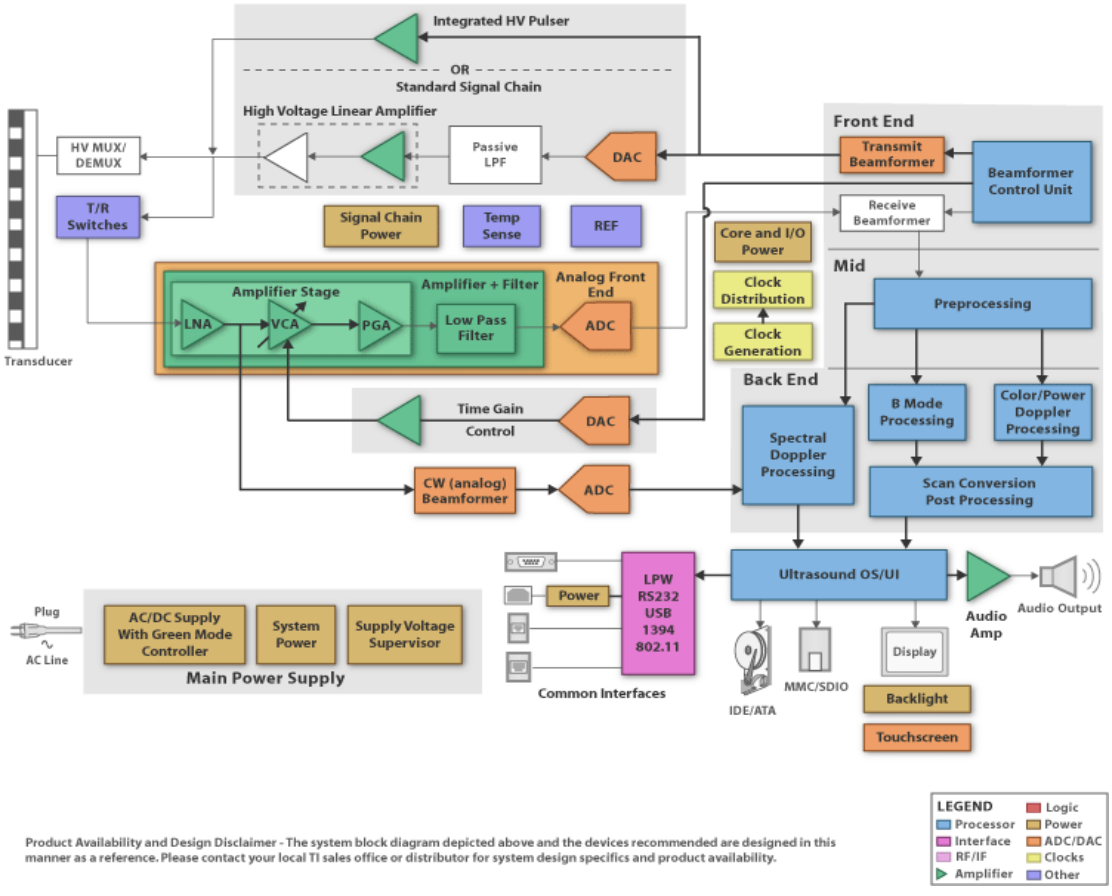

Figure 2.1. General block diagram of a medical ultrasound system as shown in Texas Instruments white paper [2]

Figure 2.1 shows the overall diagram of the ultrasound system. At first there is the transmitter and receiver part which is followed by the analog front-end that denoises and digitizes the signal. The analog front-end is followed by the signal processing block for image formation and enhancement which is divided into three parts-front-end, mid-end and back-end processing. The front-end includes the beamformer, mid-end processing includes components for filtering, detection and log compression, and the back-end includes scan conversion, speckle reduction and other processing components to enhance the image and prepare it for final display.

A critical component of the transmitter and receiver of the system is the ultrasound transducer. Each transmitter and receiver is made of an array of piezoelectric ultrasound transducer elements that transmit focused energy into the body and receive the resulting reflections. Each element is connected to the system with fine coaxial cables. High voltage multiplexing switches located in the transmitter and receiver are used to connect the number of active transducer elements required for the operation. A digital transmit beamformer generates the proper time-delayed and phase shifted digital excitation signal to form a focused transducer signal. The signals are then converted into analog signals and after being amplified using low-noise-amplifiers (LNAs), excite the transducer elements. The excited piezoelectric transducer elements convert the electrical energy into high frequency acoustical energy. An acoustical impedance matched layer of the transducer and a conducting gel is used to help the generated focused sound wave penetrate the human body. The sound wave propagates through different tissue layers and gets reflected. Due to the nonlinear nature of the human body, the signal experiences frequency-dependent attenuation and loses energy after going a certain distance. The reflected returns from the tissue boundaries are received at the receiver transducer array and are converted into electrical signals by the transducer elements. These signals are then forwarded to the analog front-end of the system.

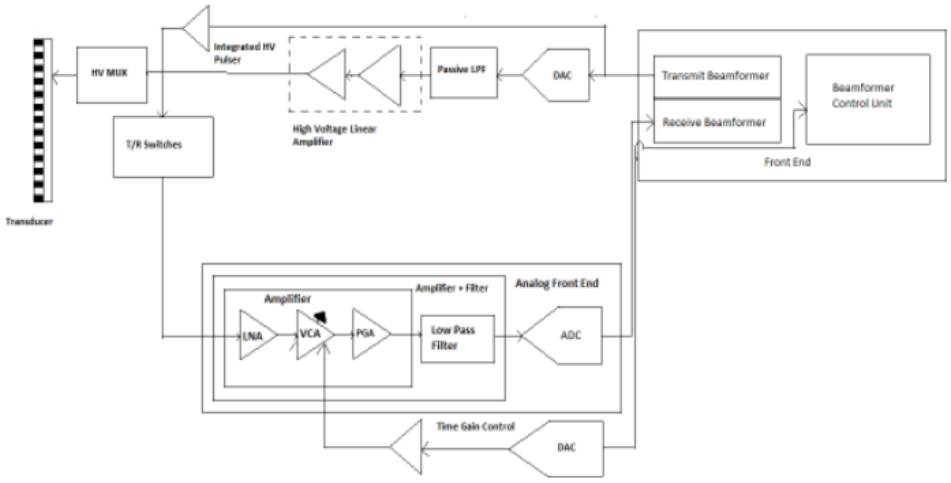

Figure 2.2. The portion of ultrasound analog front-end and beamformer we are working on

The analog front-end of the ultrasound system is a sophisticated part consisting of analog signal processing components like Low-Noise-Amplifiers (LNAs), Time Gain Compensation (TGC) amplifiers that remove noise and distortion in the signal, and Analog to Digital Converters (ADCs) that digitize the analog receive signals. The received signals are processed by the LNAs to denoise and add sufficient gain to the signals. Then, a Variable-Gain Amplifier (VGA) is used to compensate for the frequency attenuation experienced by the signal and to help to map the signal to get the dynamic range required for the ADC. An Anti-Aliasing Filter (AAF) is used to remove any high-frequency noise and interference from the signal and preserve the time-domain response of the signal.

The signal is then converted into digital form by the ADC with acceptable cost and power levels for further processing. The ADC used in this application is typically a 12-bit device running from 40Msps to 60Msps. The existing system can generate up to several Gigabytes of quantizer samples per second. Increase in the image dynamic range can require an ADC converter with more bit capacity and thus can further complicate the analog front-end.

The digitized signal output from the ADC is then beamformed in the beamformer. Although both analog and digital beamformers exist, most systems use digital beamformers. The beamforming control unit applies the appropriate time delays to the received aperture signals from an aperture, and then the beamformer sums the delayed signal to generate the beamformed signal. The beamformed signals are then processed further in the front-end, mid-end and back-end blocks to convert them into a format that is suitable to display on a CRT monitor for diagnostic purposes.

CHAPTER 3

INVESTIGATION BASED ON PREVIOUS WORKS

3.1 Previous Works on Compression and Beamforming of Ultrasound Signals

Much work has been done for the development of both lossless and lossy compression schemes for ultrasound signals. Lossy compression reduces the number of samples at the cost of sacrificing image quality; which might not be acceptable to the ultrasound practitioners. Lossless compression provides great image quality but not great compression. As medical imaging practitioners are sensitive to any error introduced in the processing, there is always a trade-off between how much error due to compression can be tolerated to retain the desired image quality.

Previous work on lossless compression of ultrasound RF data includes [7] from researchers at Texas Instruments. The authors exploited the high correlation between successive image lines and achieved a lossless compression of 2:1-3:1. They used a delay-and-subtract procedure to have destructive interference and significantly reduce the power of the adjacent lines. The residual data needs fewer bits to encode and thus results in compression. In another paper [8], the same researchers achieved a 6:1 lossy compression by exploiting correlation between adjacent signals in both lateral and axial direction. The decorrelation in the lateral direction is done using Discrete Cosine Transform or Hadamard Transform. The decorrelation in the axial direction is done using customized orthogonal wavelet packets that are optimized for a particular ultrasound probe. The paper in [3] discusses a compressive sensing approach for compressing raw ultrasound RF signals using only 10%-50% samples. They used

recently introduced directional wave atoms as basis for sparse representation of sub-sampled RF signals. The paper in [13] discusses the application of finite rate of innovation framework to ultrasound imaging that can reduce the sampling rate by 2 orders of magnitude. They derived a condition on the sampling kernel which allows perfect reconstruction of periodic streams from a minimal number of samples. However, this work imposes severe assumptions on the nature of the received signals, and only represents large signal impulses; the part of the signal due to scattering, which is also considered informative by medical practitioners, is discarded.

There has been a volume of work on beamforming as well. As beamforming is an irreversible process it is a challenge to combine the RF signals in an optimal way to preserve the diagnostic information they contain. The paper in [1] discusses different beamforming approaches like delay-and-sum beamforming, phase-matched beamforming, amplitude matched beamforming, 1D matched filtered beamforming, 2D matched-filtered (2DMF) beamforming, etc. Under the assumption that acquisition noise is well described as an additive wideband Gaussian white-noise process, they showed that signal compression across receive-aperture channels after a 2D matched-filtering operation results in no loss of diagnostic information.

3.2 The Compression Approaches We Investigated

To find an optimal compression approach, we investigated the existing compression approaches without assuming any model for the ultrasound signal. Then we developed a model for the ultrasound signal and derived the optimal basis for compression.

We tried some of the approaches mentioned above. We could not use the lossless compression approach developed in [7] as it was not applicable for real-time compression. The sampling scheme in [13] requires the prior knowledge of the number of peaks in the RF signal in question. In our trials, it showed good results when we had knowledge of the number of peaks in the signal beforehand. But in a real-time

ultrasound signal, we do not know the number of peaks beforehand, and in our trials if we assumed an incorrect number of peaks the method performed poorly. Hence, we did not further investigate that approach.

The following section discusses the compression approaches we investigated. We used peak-signal-to-noise ratio ($PSNR$) and compression ratio (CR) as measures of the compression performance those have been used other researchers previously.

The compression ratio (CR) is defined as

$$CR = 100 \times \frac{\text{no. of non-zero coefficients used for reconstruction}}{\text{total no. of coefficients}} \tag{3.1}$$

$PSNR$ is the peak signal-to-noise ratio, defined as

$$PSNR = \log_{10}\left(\frac{x_{max}}{\sqrt{MSE}}\right) \tag{3.2}$$

Where $x_{\max}$=maximum amplitude of the signal

For a signal x and its approximation x_r, the Mean Squared Error (MSE) is defined as

$$MSE = \frac{\sum_N \sum_M (x - x_r)^2}{M \times N} \tag{3.3}$$

3.2.1 Principal Component Analysis

In our preliminary stages of investigation we used Principal Component Analysis (PCA), which is a simple non-parametric method for reducing high dimensional data to lower dimension. PCA was a suitable option as it uses the data itself to generate a basis without assuming any model.

Principal Component Analysis (PCA) converts a set of observations of possibly correlated variables into a set of values of uncorrelated variables called principal components. PCA helps to identify the most meaningful basis to re-express a data set. This helps to filter out noise and reveal the hidden structure. Our goal in

investigating PCA was to get some idea of the degree of compression that might be possible.

We generated the PCA by calculating the eigenvector decomposition of the (empirical) covariance matrix for a given set of data. The tutorial in [10] discusses the procedure for PCA calculation. Assume we have a data set $\mathbf{x} = [x_1, \ldots, x_n]^T$ with covariance matrix C_X. The matrix C_X can be calculated by

$$C_X = \frac{1}{n}(\mathbf{x} - \mu_X)(\mathbf{x} - \mu_X)^T \tag{3.4}$$

where μ_X =mean of $\mathbf{x}$

$(x - \mu_X)^T$= transpose of $(\mathbf{x} - \mu_X)$

Let the eigenvectors of C_X be arranged as column vectors of the matrix Φ. Then the PCA coefficients for a given signal x found by projecting the data set onto the subspace created by the eigenvectors can be calculated by

$$c = \Phi^T x \tag{3.5}$$

To get compression, we threshold the coefficients to get a coefficient vector c_r and the approximation of the signal is recovered using

$$x_r = \Phi c_r \tag{3.6}$$

For the following example, we used a 250 sample window of an ultrasound cyst phantom data set generated using a 65 element transducer array with a carrier frequency of 3MHz. The sampling frequency was 100MHz. The number of PCA coefficients needed to reconstruct the signal set with 0.01% MSE was 16.8% of the total number of samples.

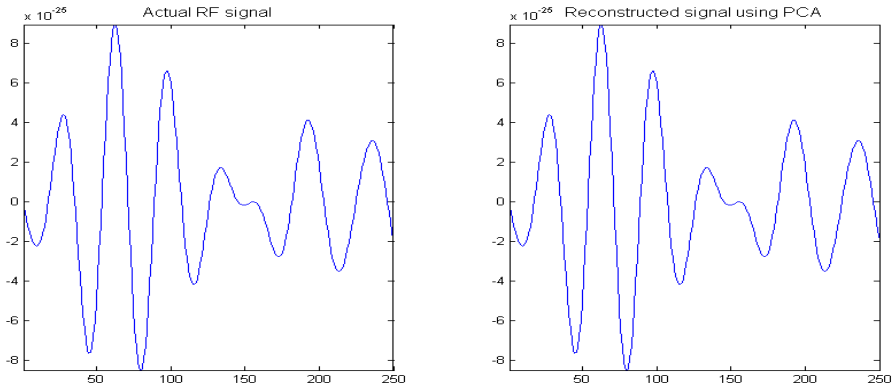

Figure 3.1. Comparison of RF signal and reconstructed signal using PCA

Table 3.1. Compression using PCA

Energy Conserved	Compression Ratio	PSNR(dB)
99.99	5.9524	48.1486

Figure 3.1 shows the comparison of actual RF signal and reconstructed signal using PCA. The following table shows the performance of compression using PCA.

Although PCA finds the best basis for compression, eigenvalue-eigenvector decomposition in real-time is difficult. As we are working on a real-time implementation, we cannot use PCA for compression.

3.2.2 Compression using Bandpass Prolate Spheroidal Functions (BPSFs)

For the next compression approach we decided to choose an appropriate basis that matches the properties of RF signals. Due to the nonlinear nature of the human body, the generated ultrasound signal shows frequency-dependent attenuation and loses energy after going a certain distance, and thus can be assumed as a time-limited signal. After denoising, we can consider the signal to be bandlimited as well.

The well-known paper by Slepian [11] discusses approximately the properties of the Prolate Spheroid Wave Functions that can be considered as both time and band-limited within certain interval. Prolate spheroids ϕ_n are defined with respect

to a finite interval $t \in [-l, l]$ and a frequency interval $f \in (-B, B)$. They form an orthogonal and complete set for functions in $L_2(-\infty, \infty)$ that are bandlimited to $f \in (-B, B)$.

$$\int_{-\infty}^{\infty} \phi_n(t)\phi_m(t)dt = \delta_{nm} \tag{3.7}$$

They also form an orthogonal and complete set in $L_2(-l, l)$.

$$\int_{-l}^{l} \phi_n(t)\phi_m(t)dt = \lambda_n \delta_{nm} \tag{3.8}$$

where λ_n is the fraction of the energy of ϕ_n that lies in the interval $(-l, l)$.

An important property of prolate spheroids is that among all the orthogonal sets $L_2(-l, l)$, prolate spheroids have the highest energy concentration in the band of frequencies $f \in (-B, B)$ with respect to which they are defined.

The bandlimited and time-limited natures of these functions match the properties of several types of signals seen in practice. For example, they have already been used as a basis for the compression of EEG signals [9] with very good results.

The prolates discussed by Slepian were lowpass in nature, but we need a basis that has the additional property of a bandpass spectrum like the modulated ultrasound signal. The paper in [6] discusses Bandpass Prolate Spheroidal Functions (BPSF) which are bandpass analogues of the prolate spheroids. We applied the BPSFs for lossy compression of the ultrasound signals. These BPSFs are the eigenfunctions ϕ_n(t) of the following equation

$$\lambda\phi(x) = \int_{-l}^{l} S_0(x - x')\phi(x')dx' \tag{3.9}$$

where

$$S_0(x - x') = \text{sinc}[2B_0(x - x')] \cos[2\pi f_0(x - x')] \tag{3.10}$$

B_0=Bandwidth of the signal

f_0=center frequency of the signal.

If we have a data vector $x \in \Re^n$ and have a matrix Φ with BPSFs as the column vectors, then we get the coefficients using equation (3.2) and after thresholding the coefficients we can recover the sparse approximation of the signal using equation (3.3).

For this example we used the same cyst phantom data we used for compression using PCA. We calculated the compression for 99.99% energy conservation in the reconstructed signal. For the calculation of BPSF we used a bandwidth B_0 =4MHz and center frequency f_0 =3MHz. Table **??** shows the compression performance of BPSF for reconstructing the RF signal.

Table 3.2. Compression using BPSF

Energy Conserved	Compression Ratio	PSNR(dB)
99.99	2.8857	49.8881

Figure 3.2 shows the comparison of a signal with the reconstructed signal using BPSFs. The time interval is 250 samples at 100MHz sampling rate, that is, $2l = 2.5\mu$s.

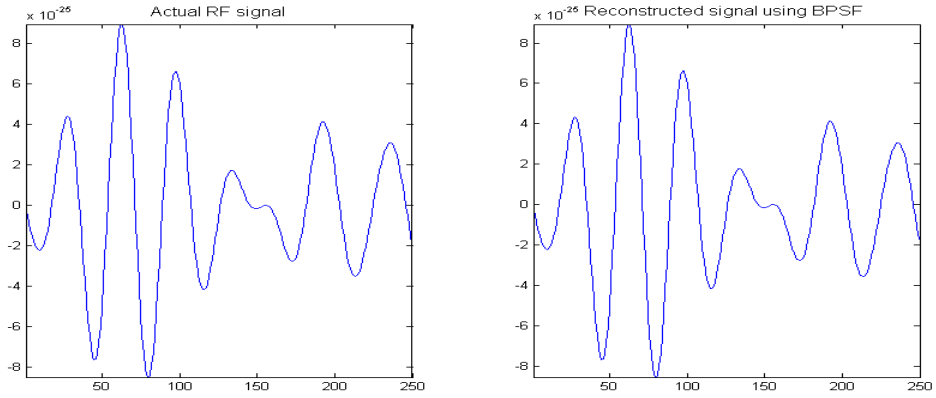

Figure 3.2. Reconstruction of ultrasound RF signal using BPSF

The sinc in kernel in (3.7) controls the time interval over which the prolate spheroids can be considered to be concentrated and it depends on the inverse of the bandwidth of the signal. As the bandwidth of ultrasound signals is in the MHz range, the BPSF tends to die out after a couple μs time interval and forces us to limit our processing to small time intervals only.

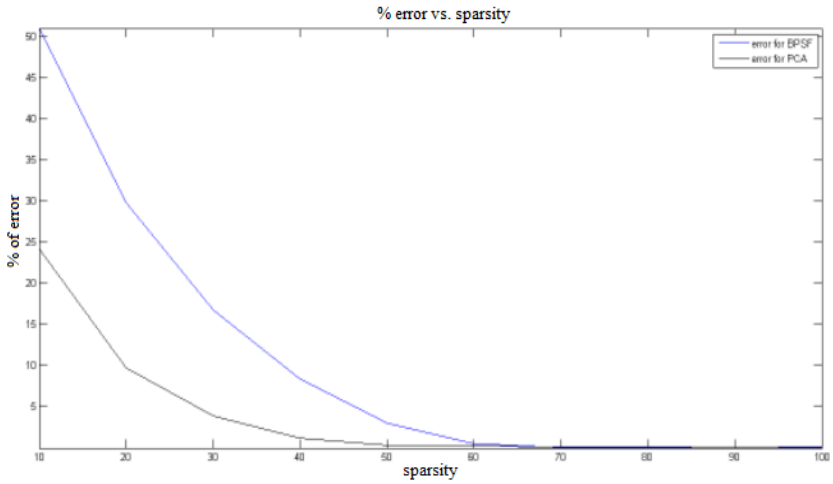

Figure 3.3. Comparison of compression performance using PCA and BPSF for various sparsity levels

Figure 3.3 shows the comparison between performance of compression using PCA and BPSF for various levels of sparsity. From the figure, we can see that PCA performs better than BPSF for all levels of sparsity. For this we used signals from 65 transducers.

3.2.3 Wavelet and Wavelet Packet Decomposition

We then analyzed our signals with wavelets, which is one of the most powerful tools used in signal processing. Wavelet decomposition uses scaled and shifted versions of a mother wavelet to decompose a signal into its high and low frequency components. A good amount of compression can be achieved if a signal can be expressed as a combination of only a couple of scaled versions of the mother wavelet.

As an ultrasound signal can be thought of as a superposition of scaled and shifted versions of the transmitted pulse, wavelet decomposition can be expected to provide good compression. The paper in [14] used the same idea to filter ultrasound signals using wavelets.

During a level 1 decomposition using wavelets, the signal is divided into low and high-frequency components. For further levels of decomposition, the low frequency part is divided into low and high-frequency parts and the high-frequency part remains intact. During wavelet packet decomposition, both the low and high frequency spectrum are further divided.

For testing, we used a phantom cyst data set generated using the Field II simulation program [5]. We took a block of 250×65 signal points reflected from the cyst phantom and did level-4 wavelet decomposition using Daubechies 10, Coiflet 5, Symlet 6 and Symlet 8 wavelets. We chose these wavelets as they are short-duration pulses just like the ultrasound pulse. We used the MATLAB built-in GUI for both 1D and 2D wavelet and wavelet packet decomposition. We used a level-4 decomposition in all cases. The coefficients found during decomposition were thresholded and the signal was reconstructed using the remaining coefficients.

In the methods described above, we compressed the signal in 1D only, i.e., we just compressed the individual received transducer signals in an aperture. The results we found from the 2D wavelet decomposition showed the compression ratio can be improved by exploiting the correlation in the received signal in successive transducer elements. As the ultrasound signal is a bandpass signal, wavelet packet decomposition showed better performance.

Tables 3.3-3.6 compare the performances of different wavelet analysis approaches for the same energy conservation in the reconstruction.

Table 3.3. 1D analysis using wavelets.

Wavelet Name	% Energy Conserved	Compression Ratio	PSNR(dB)
coif5	99.99	3.4245	47.7959
db10	99.99	3.8916	47.917
sym6	99.99	3.8667	47.6305
sym8	99.99	3.8375	48.1203

Table 3.4. 1D analysis using wavelet packets.

Wavelet Name	Energy Conserved	Compression Ratio	PSNR(dB)
coif5	99.99	5.4634	48.1581
db10	99.99	5.6774	48.0814
sym6	99.99	3.9216	47.8988
sym8	99.99	4.8842	48.3023

Tables 3.3 and 3.4 show the compression performances using 1D wavelet and wavelet packet decomposition for the same energy conservation. For both cases db10 showed better performance.

Tables 3.5 and 3.6 show the compression performances using 2D wavelet and wavelet packet decomposition for the same energy conservation. In both cases sym8 showed the best result.

Table 3.5. 2D analysis using wavelets.

Wavelet Name	Energy Conserved	Compression Ratio	PSNR(dB)
coif5	99.99	4.6965	57.917
db10	99.99	4.665	57.9695
sym6	99.99	4.9396	57.9016
sym8	99.99	5.0138	57.9512

Table 3.6. 2D analysis using wavelet packets.

Wavelet Name	Energy Conserved	Compression Ratio	PSNR(dB)
coif5	99.99	8.9021	57.745
db10	99.99	8.3122	58.0143
sym6	99.99	9.6334	57.9098
sym8	99.99	10.3247	57.9246

Figure 3.4 and 3.5 show the compression performances using 1D wavelets and wavelet packet decomposition respectively. The figures show the compression performances using Daubechies 10, Coiflet 5, Symlet 6 and Symlet 8 wavelets.

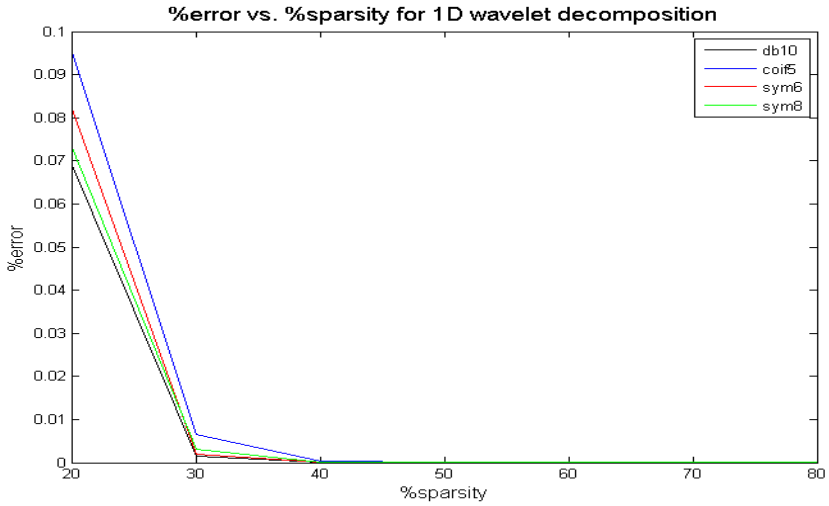

Figure 3.4. % sparsity vs % error curve for compression using 1D wavelet decomposition

From the figures we can see that for both 1D wavelet and 1D wavelet packet decomposition, db10 shows the best error performance for a given sparsity level.

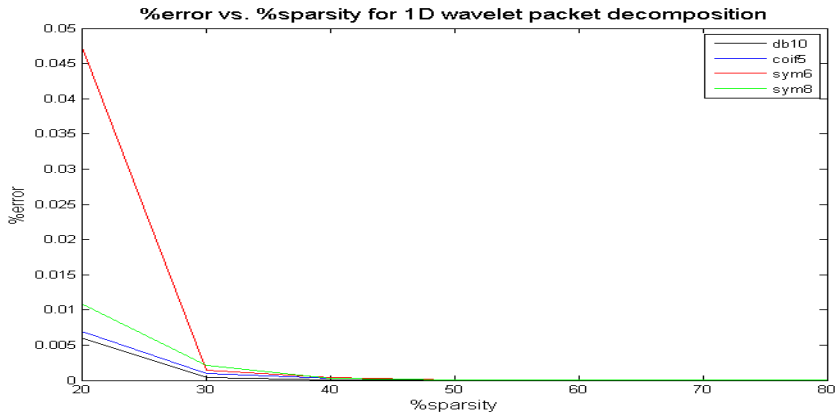

Figure 3.5. % sparsity vs % error curve for compression using 1D wavelet packet decomposition

Figure 3.6 and 3.7 show the compression performances using 2D wavelets and wavelet packet decomposition respectively. From the figure we can see that in case of 2D wavelet decomposition sym8 shows the best performance for each sparsity level. For the wavelet packet decomposition case sym8 is again showing the lowest error percentage for each sparsity level, i.e., better compression results.

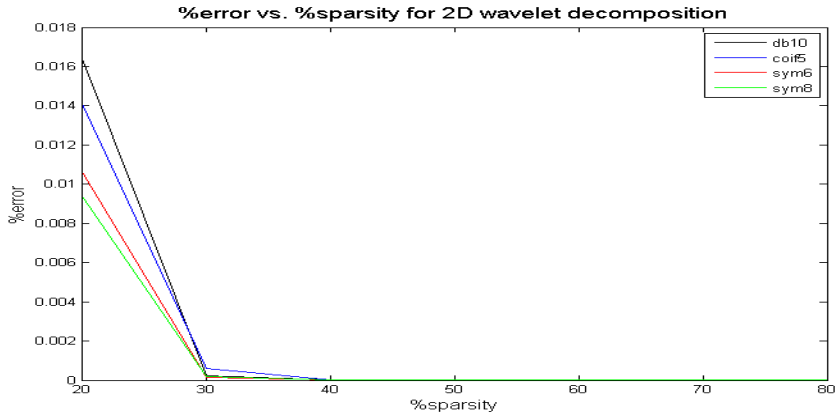

Figure 3.6. % sparsity vs % error curve for compression using 2D wavelet decomposition

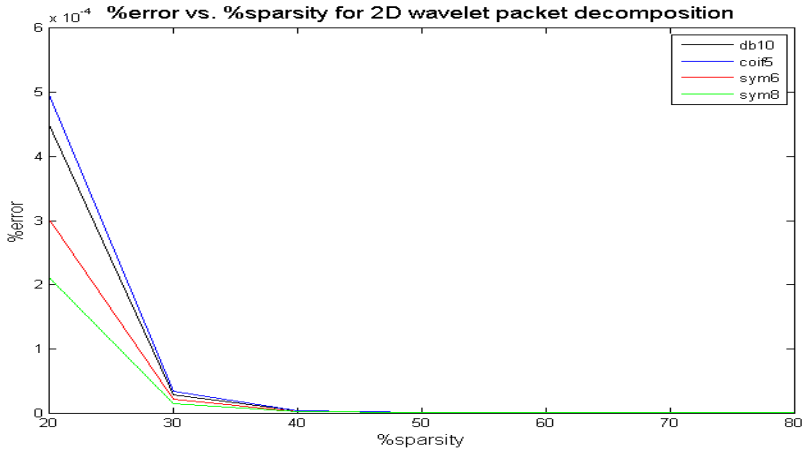

Figure 3.7. % sparsity vs % error curve for compression using 2D wavelet packet decomposition

3.2.4 2D Fourier Transform

Finally, we investigated the compression performance of the 2D Fourier Transform. We took a block of signal points and applied the Fourier Transform both in axial and lateral directions on it. The motivation behind using Fourier Transform was Karhunen-Loève Transform (KLT) of the received signals that decorrelates the signal components. In fact, it is well-known that for 2D data sets modeled as having block-circulant covariances, the KLT is the 2D DFT. The following table shows the results we found using 2D FFT for compression.

Table 3.7. Analysis using 2D FFT.

Energy Conserved	Compression Ratio	PSNR(dB)
99.99	7.1309	50.4406

The 2D FFT gave us quite good compression results, and from the implementation point of view it seems feasible. Although the 2D FFT gives us good results, it is not clear how it is related to the optimal compression scheme. So we decided to find the optimal basis using a random process model for the received ultrasound signals.

3.2.5 Our Approach: Optimal Basis for Real-Time Compression of Ultrasound RF Signals

All the work before this point was done without assuming a model for the ultrasound signal. Finally, we decided to find the optimal basis for 2D compression of the ultrasound signal starting from a model of the signal. Many models have been developed for an ultrasound RF signal. For example, the well-known paper by Jensen in [4] developed a model for the propagation and scattering of ultrasound in tissue. The expression for the received field was calculated by solving appropriate wave equations. On the other hand, the paper [15] discusses linear system models for ultrasound imaging. We found the optimal basis for compressing the ultrasound data in 2D using the concepts in [4]. This approach is described in the next chapter.

CHAPTER 4

OUR APPROACH: OPTIMAL BASIS FOR REAL-TIME COMPRESSION OF AN ULTRASOUND SIGNAL APERTURE

As mentioned previously, we are interested in the possibility of compression implemented directly on the received analog signals, so we focus on efficient real-time representations for RF signals comprising a single receive aperture. At first we derive an expression for the (time and space) autocorrelation function of the set of signals received in a linear aperture. This is then used to find the autocorrelation's eigenfunctions, which form the optimal (Karhunen-Loève) basis for compression of the aperture signal set.

We show that we can calculate the coefficients with respect to the basis by calculating Fourier Series coefficients for the received signal at each aperture element with frequencies slightly scaled by aperture position, followed by linear combinations of corresponding frequency components across the aperture. The combination weights at each frequency are determined by the eigenvectors of a matrix whose entries are averaged cross-spectral coefficients of the received signal set at that frequency. The set of coefficients larger than some threshold forms the compressed representation of the aperture signal set. We can also use the coefficients, along with the autocorrelation eigenvalues, to form a linear minimum mean-squared error (LMMSE) estimate of the reflectivity of the point scatterers along the center line (i.e. a beamformed center line).

4.1 Derivation of the Autocorrelation Function

Consider an N-element linear receive aperture centered at (lateral, elevation, axial) position $(0, 0, 0)$, with elements spaced by distance Δ in the lateral direction.

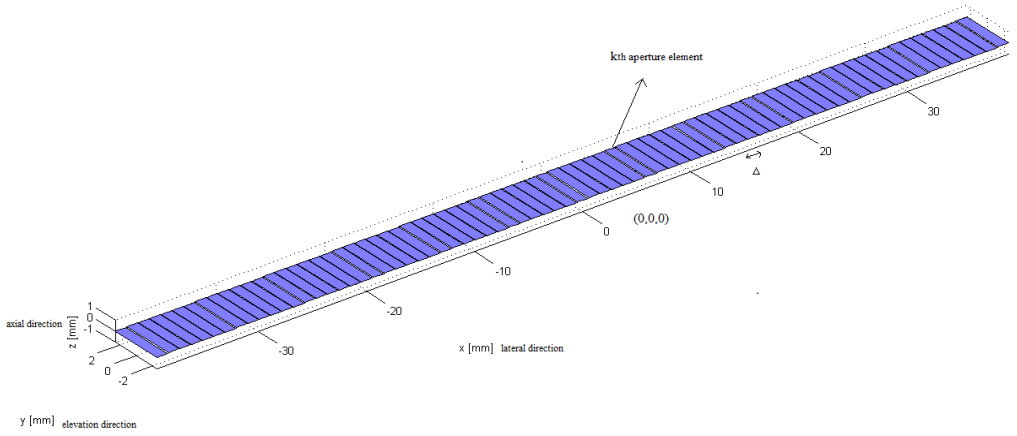

Figure 4.1. N-element linear receive aperture centered at (lateral, elevation, axial) position $(0, 0, 0)$

We assume that the transmitted pulse is focused at depth z_0 along the axial line at the aperture center. Let $x(t, k)$ denote the signal received from the focal region at the k^{th} aperture element. Jensen [4] developed a model for the received (scattered) signal at a given position in terms of the transmitted pulse (or "pulse-echo signal") and a "spatial impulse response" that characterizes the transmit/receive system in time and space. From Jensen's model for scattered signals received from the focal zone (and neglecting observation noise) we can write

$$x(t, k) = \int r(\underline{v})\{p(t) * h(k, \underline{v}, t)\}d\underline{v} \tag{4.1}$$

where $\underline{v} = (x, y, z)$ denotes spatial position; $r(\underline{v})$ is the tissue inhomogeneity field that gives rise to the scattered signal; $h(k, \underline{v}, t)$ is the spatial impulse response for receiver position $(k\Delta, 0, 0)$, object position $\underline{v}$, and time t; $p(t)$ is the pulse-echo

signal; and "*" denotes convolution in time. We further assume that the spatial impulse response can be decomposed as

$$h(k, \underline{v}, t) = g(t, (x, y), k) * \delta\Big(t - \frac{1}{c}\|\underline{v}\| - \frac{1}{c}\|(k\Delta, 0, 0) - \underline{v}\|\Big) \tag{4.2}$$

where g is a function that can vary with aperture element position, object lateral and elevation position, and time (but not with depth in the focal region); c is the speed of sound in tissue; and the impulse represents propagation time from the aperture center to $\underline{v}$ and from $\underline{v}$ to the k^{th} aperture element. This form of the spatial impulse response is consistent with experimental results shown in [5]. Define $p(t, (x, y), k) = p(t) * g(t, (x, y), k)$ and let

$$T(\underline{v}, k) = \frac{1}{c}\|\underline{v}\| + \frac{1}{c}\|(k\Delta, 0, 0) - \underline{v}\|) \tag{4.3}$$

Then

$$x(t, k) = \int r(\underline{v}) p(t - T(\underline{v}, k), (x, y), k) d\underline{v} \tag{4.4}$$

After doing the Taylor series expansion of $T(\underline{v}, k)$ around the focal point $(0, 0, z_0)$, keeping the terms up to first order in x, y and $z - z_0$, and converting the spatial variables (x, y, z) to time variables (t_1, t_2, t_3) by the relation time $= \frac{2}{c}$(space), we get

$$x(t, k) \approx \int r(t_1, t_2, t_3) p(t - T_k - \alpha_k t_3 + \beta_k t_1, (t_1, t_2), k) dt_1 dt_2 dt_3 \tag{4.5}$$

where $T_k = \frac{1}{c}\{z_0 + \sqrt{z_0^2 + (k\Delta)^2}\}, \alpha_k = \frac{1}{2}\left\{1 + \frac{z_0}{\sqrt{z_0^2 + (k\Delta)^2}}\right\}, \beta_k = \frac{1}{2}\left\{\frac{k\Delta}{\sqrt{z_0^2 + (k\Delta)^2}}\right\}$

We define the time-aligned received signals $y(t, k) = x(t + T_k, k)$ and their auto-correlation function

$$R_y([t, k]; [\tau, l]) = E\{y(t, k) y(\tau, l)\} \tag{4.6}$$

$$= \int_{\underline{v}_1} \int_{\underline{v}_2} p(t - \alpha_k t_3 + \beta_k t_1, (t_1, t_2), k) p(t - \alpha_l \tau_3 + \beta_l \tau_1, (\tau_1, \tau_2), l) \tag{4.7}$$
$$E\{r_t(t_1, t_2, t_3) r_t(\tau_1, \tau_2, \tau_3)\} dt_1 dt_2 dt_3 d\tau_1 d\tau_2 d\tau_3$$

If we assume a white noise tissue inhomogeneity field, so that

$$E\{r(t_1, t_2, t_3) r(\tau_1, \tau_2, \tau_3)\} = \sigma^2 \delta(t_1 - \tau_1, t_2 - \tau_2, t_3 - \tau_3) \tag{4.8}$$

We get

$$R_y([t,k];[\tau,l]) = \sigma^2 \int_{\underline{v}_1} p\big(t - \alpha_k t_3 + \beta_k t_1, \big(t_1, t_2\big), k\big) p\big(\tau - \alpha_l t_3 + \beta_l t_1, (t_1, t_2), l\big) dt_1 dt_2 dt_3 \tag{4.9}$$

Let $q\big(t, (t_1, t_2), k\big) = p\big(- \alpha_k t, (t_1, t_2), k\big)$ then eq. (4.9) becomes

$$R_y([t,k];[\tau,l]) = \sigma^2 \int_{\underline{v}_1} q\left(t_3 - \frac{t}{\alpha_k} - \frac{\beta_k}{\alpha_k} t_1, (t_1, t_2), k\right) q\left(t_3 - \frac{\tau}{\alpha_l} - \frac{\beta_l}{\alpha_l} t_1, (t_1, t_2), l\right) dt_1 dt_2 dt_3 \tag{4.10}$$

Let $s = t_3 - \frac{t}{\alpha_k} - \frac{\beta_k}{\alpha_k} t_1$ to get

$$\begin{aligned} R_y([t,k];[\tau,l]) =& \sigma^2 \int_{t_1} \int_{t_2} \left[\int_s q\big((t_1, t_2), s, k\big) \right. \\ & \left. q\left((t_1, t_2), s + \left[\frac{t}{\alpha_k} - \frac{\tau}{\alpha_l}\right] + \left[\frac{\beta_k}{\alpha_k} - \frac{\beta_l}{\alpha_l}\right] t_1, l\right) ds \right] dt_1 dt_2 \end{aligned} \tag{4.11}$$

As $\left[\frac{\beta_k}{\alpha_k} \approx \frac{\beta_l}{\alpha_l}\right]$ we can modify eq. (4.11) in the following way

$$R_y([t,k];[\tau,l]) \approx \sigma^2 \int_{t_1} \int_{t_2} \left[\int_s q\Big(\Big(t_1, t_2\Big), s, k\Big) q\left((t_1, t_2), s + \left[\frac{t}{\alpha_k} - \frac{\tau}{\alpha_l}\right], l\right) ds \right] dt_1 dt_2 \tag{4.12}$$

Then we define the cross-correlation function

$$c\big(b, (t_1, t_2), (k, l)\big) = \int_s q\big(s, (t_1, t_2), k\big) q\big(s + b, (t_1, t_2), l\big) ds \tag{4.13}$$

From eq. (4.12) we get

$$R_y([t,k];[\tau,l]) = \sigma^2 \int_{t_2}\int_{t_1} c\Big(\Big[\frac{t}{\alpha_k} - \frac{\tau}{\alpha_l}\Big],(t_1,t_2),(k,l)\Big)dt_1 dt_2 \tag{4.14}$$

Define

$$d(t,(k,l)) = \sigma^2 \int_{t_1}\int_{t_2} c(t,(t_1,t_2),(k,l))dt_1 dt_2 \tag{4.15}$$

Then eq. (4.14) becomes

$$R_y([t,k];[\tau,l]) = d\left(\frac{t}{\alpha_k} - \frac{\tau}{\alpha_l},(k,l)\right) \tag{4.16}$$

That is: the autocorrelation of the time-aligned received aperture signals is formed from the cross-correlations of the (time-scaled, reversed and shifted) received pulses averaged across the lateral and elevation extent of the tissue region, and the autocorrelation for samples from signals at different aperture positions depends on the difference in the sample times scaled according to the positions.

4.2 Derivation of the Optimal Basis for Compression

We now want to find the eigenfunctions and eigenvalues of the autocorrelation. Let us define $z(t,k) = \sqrt{\alpha_k}y(\alpha_k t,k)$, so $z(t,k)$ has autocorrelation

$$\begin{aligned} E\{z(t,k)z(\tau,l)\} &= R_z([t,k];[\tau,l]) \\ &= \sqrt{\alpha_k\alpha_l}R_y([\alpha_k t,k];[\alpha_l\tau,l]) \\ &= \sqrt{\alpha_k\alpha_l}d(t-\tau,(k,l)) \end{aligned} \tag{4.17}$$

Let $b(t,(k,l)) = \sqrt{\alpha_k\alpha_l}d(t,(k,l))$. Then the eigenfunctions $\phi(t,k)$ and eigenvalues η of the autocorrelation defined by (4.17) must satisfy

$$\sum_{l=0}^{N-1}\int_{-\frac{T}{2}}^{\frac{T}{2}} b(t-\tau,(k,l))\phi(\tau,l)d\tau = \eta\phi(t,k); -\frac{T}{2} \le t \le \frac{T}{2}, k = 0,\ldots,N-1 \tag{4.18}$$

Assume that for each $k, \phi(t,k)$ must be time limited to $-\frac{T}{2} \leq t \leq \frac{T}{2}$. Then we can write

$$\phi(t,k) = \sum_i \mu(i,k) p_i(t) \tag{4.19}$$

where $\{p_i(t); i = 0, 1, \dots\}$ comprise any complete orthonormal (CON) set for $L_2[-\frac{T}{2}, \frac{T}{2}]$ and $\mu(i,k) = \langle \phi(i,k), p_i \rangle$.

Now, substitute eq. (4.19) into eq. (4.18) and take the Fourier Transform (over t) of eq. (4.18). The result is

$$\sum_{l=0}^{N-1} B(f,(k,l)) \sum_{i=0}^{\infty} \mu(i,l) P_i(f) = \eta \sum_{i=0}^{\infty} \mu(i,k) P_i(f) \; ;$$
$$\text{for all } f, \; k = 0, \dots, N-1 \tag{4.20}$$

where $B(f,(k,l))$ and $P_i(f)$ are Fourier Transforms of $b(t,(k,l))$ and $p_i(t)$ respectively. Let $\underline{\mu} = \{\mu(i,k); i = 0, 1, \dots; k = 1, \dots, N-1\} \in l_2 \times [0, \dots, N-1]$. Define the linear transformation $P : l_2 \times [0, \dots, N-1] \to L_2(-\infty, \infty) \times [0, \dots, N-1]$ by $[P\underline{\mu}](f,k) = \sum_{i=0}^{\infty} \mu(i,k) P_i(f)$. Let $P^* : L_2(-\infty, \infty) \times [0, \dots, N-1] \to l_2 \times [0, \dots, N-1]$ denote the adjoint of P. Then for every $\underline{x} \in L_2(-\infty, \infty) \times [0, \dots, N-1]$ we have

$$\begin{aligned} \langle \underline{\mu}, P^* \underline{x} \rangle &= \sum_{i=0}^{\infty} \mu(i,k) \{[P^* \underline{x}](i,k)\}^* \\ &= \langle P\underline{\mu}, \underline{x} \rangle \\ &= \sum_k \int_{-\infty}^{\infty} X_k^*(f) \sum_i \mu(i,k) P_i(f) df \end{aligned} \tag{4.21}$$

which implies that

$$[P^* \underline{x}](i,k) = \int_{-\infty}^{\infty} X_k(f) P_i^*(f) df \tag{4.22}$$

So, since $\int_{-\infty}^{\infty} P_i(f)P_j^*(f)df = \langle P_i, P_j \rangle = \delta_{ij}$, we have

$$\begin{aligned}
[P^* P\underline{\mu}](j,k) &= \left[P^* \left\{ \sum_{i=0}^{\infty} \mu(i,k) P_i(f) \right\} \right](j,k) \\
&= \int_{-\infty}^{\infty} \sum_{i=0}^{\infty} \mu(i,k) P_i(f) P_j^*(f) df \\
&= \sum_{i=0}^{\infty} \mu(i,k) \int_{-\infty}^{\infty} P_i(f) P_j^*(f) df \\
&= \mu(j,k) \qquad (4.23)
\end{aligned}$$

which verifies that $P^* = P^{-1}$.

Now define an operator $B : L_2(-\infty,\infty)\times[0,\ldots,N-1] \rightarrow L_2(-\infty,\infty)\times[0,\ldots,N-1]$ by

$$[B\underline{x}](f,k) = \sum_{l=0}^{N-1} B(f,(k,l)) X_l(f) \qquad (4.24)$$

Now note: since $b(t,(k,l))$ is an autocorrelation function, it follows that B is positive definite and self-adjoint. In fact,

$$\begin{aligned}
\langle B\underline{x}, \underline{x} \rangle &= \sum_{k=0}^{N-1} \int_{-\infty}^{\infty} \left\{ \sum_{l=0}^{N-1} B(f,(k,l)) X_l(f) \right\} X_k^*(f) df \\
&= \sum_{k=0}^{N-1} \sum_{l=0}^{N-1} \int_{-\infty}^{\infty} \{ b(t,(k,l)) * x_l(t) \} x_k(t) dt \\
&= \sum_{k=0}^{N-1} \sum_{l=0}^{N-1} \int_{-\infty}^{\infty} \int_{-\infty}^{\infty} \{ b(t-\tau,(k,l)) x_l(\tau) \} x_k(t) d\tau dt \\
&= \sum_{k=0}^{N-1} \sum_{l=0}^{N-1} \int_{-\infty}^{\infty} \int_{-\infty}^{\infty} E\{ z(t,k) z(t,l) \} x_l(\tau) x_k(t) d\tau dt \\
&= E\left\{ \left[\sum_{k=0}^{N-1} \int_{-\infty}^{\infty} z(t,k) x_k(t) dt \right]^2 \right\} \geq 0 \qquad (4.25)
\end{aligned}$$

which verifies that B is positive definite. Also note that $b(t,(k,l)) = b(-t,(l,k))$, which implies that $B(f,(k,l)) = B^*(f,(l,k))$. Hence,

$$\begin{aligned}
\langle \underline{x}, B\underline{y} \rangle &= \sum_{l=0}^{N-1} \int_{-\infty}^{\infty} X_l(f) \Big[\sum_{k=0}^{N-1} B(f,(k,l)) Y_k(f) \Big]^* df \\
&= \sum_{l=0}^{N-1} \int_{-\infty}^{\infty} X_l(f) \Big[\sum_{k=0}^{N-1} B^*(f,(k,l)) Y_k(f) \Big]^* df \\
&= \sum_{k=0}^{N-1} \int_{-\infty}^{\infty} \Big[\sum_{l=0}^{N-1} B(f,(k,l)) X_l(f) \Big] Y_k^*(f) df \\
&= \langle B\underline{x}, \underline{y} \rangle \qquad (4.26)
\end{aligned}$$

which verifies that B is self-adjoint.

Now, from eq. (4.24) and the definition of P we have

$$[BP\underline{\mu}(f,k)] = \sum_{k=0}^{N-1} B(f,(k,l)) \sum_{i=0}^{\infty} \mu(i,l) P_i(f) \qquad (4.27)$$

By eq. (4.20) we have $BP\underline{\mu} = \eta P\underline{\mu}$; and since $P^* = P^{-1}$, it follows that

$$P^* BP\underline{\mu} = \eta\underline{\mu} \qquad (4.28)$$

where $P^*BP : l_2 \times [0,\ldots,N-1] \to l_2 \times [0,\ldots,N-1]$ is positive definite and self-adjoint. It's helpful to put eq. (4.28) in the form of an (infinite) vector-matrix equation. Note that

$$\begin{aligned}
[P^*BP\underline{\mu}](j,k) &= \int_{-\infty}^{\infty} \sum_{l=0}^{N-1} B(f,(k,l)) \sum_{i=0}^{\infty} \mu(i,l) P_i(f) P_j^*(f) df \\
&= \sum_{i=0}^{\infty} \Big\{ \sum_{l=0}^{N-1} \mu(i,l) \int_{-\infty}^{\infty} B(f,(k,l)) P_i(f) P_j^*(f) df \Big\} \qquad (4.29)
\end{aligned}$$

Define the N-vector $\underline{\mu_i} = \begin{bmatrix} \mu(i,0) \\ \vdots \\ \mu(i,N-1) \end{bmatrix}$, for each $i = 0,\ldots,$ and for each (j,i) define the $N \times N$ matrix $A_{ji} = \int_{-\infty}^{\infty} \underline{B}(f) P_i(f) P_j^*(f) df$ where $\underline{B}(f)$ is the $N \times N$ matrix having $(k,l)^{th}$ element $B(f,(k,l))$. Then from eqs. (4.28) and (4.29) we get

$$\sum_{i=0}^{\infty} A_{ji}\underline{\mu}_i = \eta\underline{\mu}_j; j = 0, 1, 2, \ldots \tag{4.30}$$

Finally, define the infinite vector $\underline{\mu} = \begin{bmatrix} \underline{\mu}_0 \\ \underline{\mu}_1 \\ \underline{\mu}_2 \\ \vdots \end{bmatrix}$ and let A be the (positive definite, self-adjoint) infinite block matrix having $(j,i)^{th}$ block A_{ji}. Then by eq. (4.30) we have

$$A\underline{\mu} = \eta\underline{\mu} \tag{4.31}$$

Approximate solutions to eq. (4.31) may lead to practical approximations to solutions of eq. (4.18). In particular, if we choose the basis $p_i(t)$ appropriately, we may be able to approximate the matrix A in such a way that approximate solutions to eq. (4.31) are easy to obtain.

Several bases have been proposed for compressing ultrasound signals, including orthogonal wavelet packets that are matched to transmitted pulses [8], and directional wave atoms [3]. However, it is not clear that these lead to any particularly convenient expression for A. In this work we assume that (as is typically the case in practice) the observation interval length is much greater than the inverse of the system bandwidth. In particular, we assume that $\underline{B}(f)$ is smooth over intervals that are large compared to $\frac{1}{T}$. Figure 4.2 and 4.3 demonstrates this property for the values of $k = 11, l = 11$ and $k = 13, l = 15$ respectively.

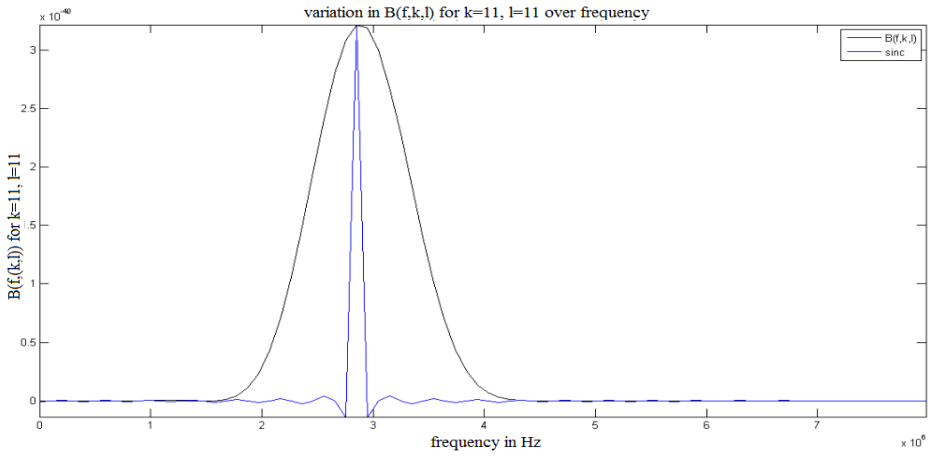

Figure 4.2. Demonstration of the smoothness of $B(f,(k,l))$ for $k = 11, l = 11$

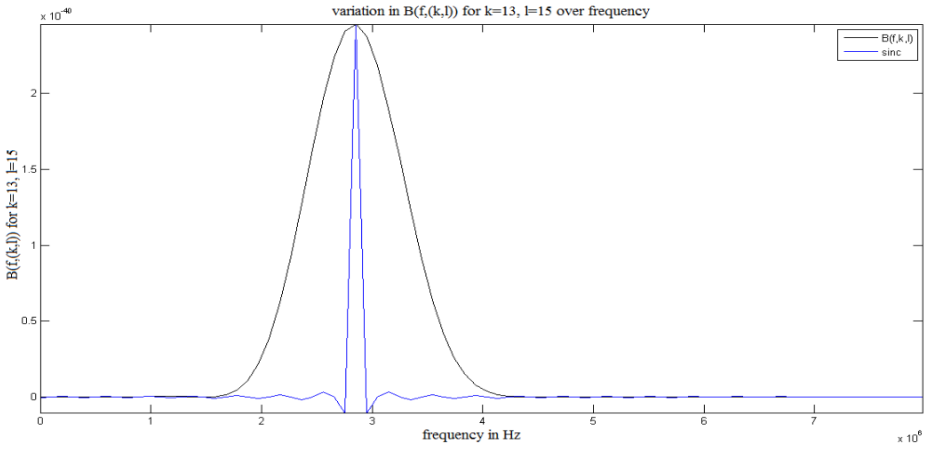

Figure 4.3. Demonstration of the smoothness of $B(f,(k,l))$ for $k = 13, l = 15$

We use the Fourier Series basis

$$p_0(t) = \frac{1}{\sqrt{T}}\text{rect}\left(\frac{t}{T}\right)$$

$$p_i(t) = \begin{cases} \sqrt{\frac{2}{T}}\sin\left(\pi\frac{i+1}{T}t\right)\text{rect}\left(\frac{t}{T}\right), & i \text{ odd}, \ i{>}0 \\ \sqrt{\frac{2}{T}}\cos\left(\pi\frac{it}{T}\right)\text{rect}\left(\frac{t}{T}\right), & i \text{ even}, i > 0 \end{cases} \tag{4.32}$$

where $\text{rect}(x) = \begin{cases} 1, & |x| < \frac{1}{2} \\ 0, & \text{otherwise} \end{cases}$

Then we get

$$P_0(f) = \sqrt{T}\text{sinc}(fT)$$

$$P_i(f) = \begin{cases} \frac{1}{j}\sqrt{\frac{T}{2}}\Big\{\text{sinc}\Big(T\Big[f - \frac{i+1}{2T}\Big]\Big) - \text{sinc}\Big(T\Big[f + \frac{i+1}{2T}\Big]\Big)\Big\}, & i \text{ odd}, i > 0 \\ \sqrt{\frac{T}{2}}\Big\{\text{sinc}\Big(T\Big[f - \frac{i}{2T}\Big]\Big) + \text{sinc}\Big(T\Big[f + \frac{i}{2T}\Big]\Big)\Big\}, & i \text{ even}, i > 0 \end{cases} \tag{4.33}$$

It follows that

$$\begin{aligned} A_{00} &= \int_{-\infty}^{\infty} \underline{B}(f)T\text{sinc}^2(fT)df \\ &\approx \underline{B}(0) \end{aligned} \tag{4.34}$$

and for i odd, $i > 0$

$$\begin{aligned} A_{i,i} &= A_{i+1,i+1} \\ &\approx \int_{-\infty}^{\infty} \underline{B}(f)\frac{T}{2}\Big\{\text{sinc}^2\Big(T\Big[f - \frac{i+1}{2T}\Big]\Big) + \text{sinc}^2\Big(T\Big[f + \frac{i+1}{2T}\Big]\Big)\Big\}df \\ &\approx \frac{1}{2}\Big\{\underline{B}\Big(\frac{i+1}{2T}\Big) + \underline{B}\Big(-\frac{i+1}{2T}\Big)\Big\} \\ &= \Re\Big\{\underline{B}\Big(\frac{i+1}{2T}\Big)\Big\} \end{aligned} \tag{4.35}$$

$$\begin{aligned} A_{i,i+1} &= -A_{i+1,i} \\ &\approx j\int_{-\infty}^{\infty} \underline{B}(f)\frac{T}{2}\Big\{\text{sinc}^2\Big(T\Big[f - \frac{i+1}{2T}\Big]\Big) - \text{sinc}^2\Big(T\Big[f + \frac{i+1}{2T}\Big]\Big)\Big\}df \\ &\approx \frac{j}{2}\Big\{\underline{B}\Big(\frac{i+1}{2T}\Big) - \underline{B}\Big(-\frac{i+1}{2T}\Big)\Big\} \\ &= -\Im\Big\{\underline{B}\Big(\frac{i+1}{2T}\Big)\Big\} \end{aligned} \tag{4.36}$$

$$A_{i,l} \approx 0, \text{for all other } (i,l) \tag{4.37}$$

So, the matrix A in eq. (4.31) can be approximated by the (positive definite, self-adjoint) infinite block diagonal matrix.

$$\tilde{A} = \begin{bmatrix} \underline{B}(0) & & & & \\ & \Re\Big\{\underline{B}\Big(\frac{1}{2T}\Big)\Big\} & -\Im\Big\{\underline{B}\Big(\frac{1}{2T}\Big)\Big\} & & \\ & \Im\Big\{\underline{B}\Big(\frac{1}{2T}\Big)\Big\} & \Re\Big\{\underline{B}\Big(\frac{1}{2T}\Big)\Big\} & & \\ & & & \Re\Big\{\underline{B}\Big(\frac{2}{2T}\Big)\Big\} & -\Im\Big\{\underline{B}\Big(\frac{2}{2T}\Big)\Big\} \\ & & & \Im\Big\{\underline{B}\Big(\frac{2}{2T}\Big)\Big\} & \Re\Big\{\underline{B}\Big(\frac{2}{2T}\Big)\Big\} \\ & & & & \cdots \quad \cdots \end{bmatrix}$$

Let $\{\eta^{(i)}, i = 0, 1, \dots\}$ denote the eigenvalues of $\tilde{A}$, with $\{\underline{\mu}^{(i)}, i = 0, 1, \dots\}$ being a corresponding orthonormal set of eigenvectors. We can specify these as follows: Let $\{\lambda_0, \dots, \lambda_{N-1}\}$ denote the eigenvalues of $\underline{\mathrm{B}}(0)$, with $\{\underline{\gamma}_0, \dots, \underline{\gamma}_{N-1}\}$ being a corresponding orthonormal set of eigenvectors; and for $m = 1, 2, \dots$, let $\{\sigma_{m,0}, \dots, \sigma_{m,2N-1}\}$ denote the eigenvalues of $\begin{bmatrix} \Re\{\underline{B}(\frac{m}{2T})\} & -\Im\{\underline{B}(\frac{m}{2T})\} \\ \Im\{\underline{B}(\frac{m}{2T})\} & \Re\{\underline{B}(\frac{m}{2T})\} \end{bmatrix}$ with $\{\underline{\nu}_{m,0}, \dots, \underline{\nu}_{m,2N-1}\}$ being a corresponding orthonormal set of eigenvectors. Then we can set:

(i) For $i = 0, \dots, N-1$

$$\eta^{(i)} = \lambda_i$$
$$\mu^{(i)}(l) = \begin{cases} \gamma_i(l), & l = 0, \dots, N-1 \\ 0, & \text{otherwise} \end{cases} \tag{4.38}$$

(ii) For $i = (2m-1)N + n, m = 1, 2, \dots; n = 0, 1, \dots, 2N-1$

$$\eta^{(i)} = \sigma_{mn}$$
$$\mu^{(i)}(l) = \begin{cases} \nu_{mn}(l), & l = (2m-1)N, \ldots, (2m+1)N-1 \\ 0, & \text{otherwise} \end{cases} \tag{4.39}$$

Now, let $\{\eta_{0n}, n = 0, 1, \ldots, N-1\} \cup \{\eta_{mn}, m = 1, 2, \ldots; n = 0, 1, \ldots, 2N-1\}$ denote the eigenvalues of the autocorrelation of eq. (4.17) and $\{\phi_{0n}, n = 0, 1, \ldots, N-1\} \cup \{\phi_{mn}, m = 1, 2, \ldots; n = 0, 1, \ldots, 2N-1\}$ being a corresponding orthonormal set of eigenfunctions. Then from eqs. (4.19), (4.32), (4.38) and (4.39), it follows that these (approximately) have the form:

(i) for $n = 0, \ldots, N-1$

$$\begin{aligned} \eta_{0n} &= \lambda_n \\ \phi_{mn}(t,k) &= \frac{1}{\sqrt{T}}\gamma_n(k), \\ &\text{for } k = 0, 1, \ldots, N-1; |t| \leq \frac{T}{2} \end{aligned} \tag{4.40}$$

(ii) for $m = 1, 2, \ldots; n = 0, 1, \ldots, 2N-1$

$$\begin{aligned} \eta_{mn} &= \sigma_{mn} \\ \phi_{mn}(t,k) &= \sqrt{\frac{2}{T}}\left[\nu_{mn}(k)\sin\left(2\pi\frac{m}{T}t\right) + \nu_{mn}(k+N)\cos\left(2\pi\frac{m}{T}t\right)\right] \\ &\text{for } k = 0, 1, \ldots, N-1;\ |t| \leq \frac{T}{2} \end{aligned} \tag{4.41}$$

Finally, we can define eigenvalues $\{\lambda_{mn}\}$ and corresponding eigenfunctions $\{\psi_{mn}(t,k)\}$ for the autocorrelation function (given by eq. (4.16)) for the aperture signal set $\{y(t,k)\}$:

$$\begin{aligned} \lambda_{mn} &= \sigma_{mn} \\ \psi_{mn}(t,k) &= \frac{1}{\sqrt{\alpha_k}}\phi_{mn}\left(\frac{t}{\alpha_k}\right), k = 0, 1, \ldots, N-1; |t| \leq \frac{\alpha_k T}{2} \end{aligned} \tag{4.42}$$

We can verify that $\{\psi_{mn}(t,k)\}$ is an orthonormal set in $L_2[-\frac{\alpha_0 T}{2}, \frac{\alpha_0 T}{2}] \times \cdots \times L_2[-\frac{\alpha_{N-1} T}{2}, \frac{\alpha_{N-1} T}{2}]$:

$$\langle \psi_{nm}(t,k), \psi_{ij}(t,k) \rangle = \sum_{k=0}^{N-1} \int_{-\frac{\alpha_k T}{2}}^{\frac{\alpha_k T}{2}} \psi_{mn}(t,k)\psi_{ij}(t,k)dt$$

$$= \sum_{k=0}^{N-1} \int_{\frac{-\alpha_k T}{2}}^{\frac{\alpha_k T}{2}} \sqrt{\frac{2}{\alpha_k T}} \left\{ \nu_{mn}(k) \sin\left(\frac{2\pi mt}{\alpha_k T}\right) + \nu_{mn}(k+N) \cos\left(\frac{2\pi mt}{\alpha_k T}\right) \right\}$$

$$\sqrt{\frac{2}{\alpha_k T}} \left\{ \nu_{ij}(k) \sin\left(\frac{2\pi it}{\alpha_k T}\right) + \nu_{ij}(k+N) \cos\left(\frac{2\pi it}{\alpha_k T}\right) \right\} dt \qquad (4.43)$$

from which it follows that

$$\langle \psi_{mn}, \psi_{ij} \rangle = 0, i \neq m; \qquad (4.44)$$

For $i = m$;

$$\langle \psi_{mn}(t,k), \psi_{mj}(t,k) \rangle$$

$$= \sum_{k=0}^{N-1} \int_{\frac{-\alpha_k T}{2}}^{\frac{\alpha_k T}{2}} \sqrt{\frac{2}{\alpha_k T}} \left\{ \nu_{mn}(k) \sin\left(\frac{2\pi mt}{\alpha_k T}\right) + \nu_{mn}(k+N) \cos\left(\frac{2\pi mt}{\alpha_k T}\right) \right\}$$

$$\sqrt{\frac{2}{\alpha_k T}} \left\{ \nu_{mj}(k) \sin\left(\frac{2\pi mt}{\alpha_k T}\right) + \nu_{mj}(k+N) \cos\left(\frac{2\pi mt}{\alpha_k T}\right) \right\} dt$$

$$= \sum_{k=0}^{N-1} \frac{2}{\alpha_k T} \int_{\frac{-\alpha_k T}{2}}^{\frac{\alpha_k T}{2}} \left\{ \nu_{mn}(k) \sin\left(\frac{2\pi mt}{\alpha_k T}\right) + \nu_{mn}(k+N) \cos\left(\frac{2\pi mt}{\alpha_k T}\right) \right\}$$

$$\left\{ \nu_{mj}(k) \sin\left(\frac{2\pi mt}{\alpha_k T}\right) + \nu_{mj}(k+N) \cos\left(\frac{2\pi mt}{\alpha_k T}\right) \right\} dt$$

$$= \sum_{k=0}^{N-1} \left\{ \nu_{mn}(k)\nu_{mj}(k) + \nu_{mn}(k+N)\nu_{mj}(k+N) \right\}$$

$$= \sum_{k=0}^{2N-1} \nu_{mn}(k)\nu_{mj}(k)$$

$$= \begin{cases} 1, & j = n \\ 0, & j \neq n \end{cases}$$

The signal set coefficients with respect to the basis $\{\psi_{mn}\}$(that is, the KLT coefficients of the aperture signal set) are given by

For $m = 0; n = 0, \ldots, N-1$

$$\begin{aligned} y_{mn} &= \langle y, \psi_{mn} \rangle \\ &= \sum_{k=0}^{N-1} \int_{\frac{-\alpha_k T}{2}}^{\frac{\alpha_k T}{2}} y(t,k)\psi_{mn}(t,k)dt \\ &= \sqrt{\frac{1}{\alpha_k T}} \sum_{k=0}^{N-1} \gamma_n(k) \int_{\frac{-\alpha_k T}{2}}^{\frac{\alpha_k T}{2}} y(t,k)dt \end{aligned}$$

For $m = 1, 2, \ldots; n = 0, 1, \ldots, 2N-1$

$$\begin{aligned} y_{mn} = \sqrt{\frac{2}{\alpha_k T}} \sum_{k=0}^{N-1} \Bigg\{ & \nu_{mn}(k) \int_{\frac{-\alpha_k T}{2}}^{\frac{\alpha_k T}{2}} y(t,k) \sin\left(\frac{2\pi m t}{\alpha_k T}\right) dt + \\ & \nu_{mn}(k+N) \int_{\frac{-\alpha_k T}{2}}^{\frac{\alpha_k T}{2}} y(t,k) \cos\left(\frac{2\pi m t}{\alpha_k T}\right) dt \Bigg\} \end{aligned} \tag{4.45}$$

That is, the coefficients are calculated by first finding the real and imaginary part of Fourier Series coefficients of the received aperture signals (at frequencies scaled according to aperture position). Then the real and imaginary parts of the Fourier Series coefficients at the m^{th} frequency are multiplied by weights $\nu_{mn}(k)$ and $\nu_{mn}(k+N)$, respectively, which are components of eigenvectors of the m^{th} diagonal block of $\tilde{A}$, and summed across the aperture.

The aperture signal approximations that would be reconstructed from a set of KLT coefficients have the form

$$\hat{y_k}(t,k) = \sum_n \sum_m y_{mn}\psi_{mn}(t,k) \tag{4.46}$$

4.3 LMMSE Estimation of Tissue Reflectivity Using the Optimal Basis

The $\{y_{mn}\}$ calculated can be used for estimating the linear minimum mean-squared error (LMMSE) estimate of the reflectivity of the point scatterers on the scan line; in other words, for generating the beamformed signal at the aperture center using the LMMSE estimate.

Let $\underline{r_0} = \left\{ r(0,0,z), |z - z_0| \leq \frac{cT}{4} \right\}$ denote the portion of the scattering field that we wish to estimate based on the received signals $\underline{y} = \{y(t,k)\}$. It is well known [12] that the LMMSE estimate of $\underline{r_0}$, given $\underline{y}$, has the form

$$\underline{\hat{r_0}} = R_{r_0 y} R_y^{-1} y \tag{4.47}$$

where $R_{r_0 y}$= cross-correlation of $\underline{r_0}$ and $\underline{y}$

R_y=autocorrelation of $\underline{y}$

Assume that $\underline{y}$ satisfies our model given in section (4.1), along with added observation noise. Then with the eigenfunctions found in section (4.2) we can write

$$\underline{y} = \sum_n \sum_m y_{mn} \underline{\psi}_{mn} + \underline{n} \tag{4.48}$$

where $\underline{\psi}_{mn} = \{\psi_{mn}(t,k)\}$=$(m,n)^{th}$ eigenfunction

$\underline{n} = \{n(t,k)\}$=observation noise assumed to be white with variance σ_N^2

Then with respect to the basis $\{\psi_{mn}\}, R_y$ is diagonal with eigenvalues $\rho_{mn} = \lambda_{mn} + \sigma_N^2$ where λ_{mn} is the $(m,n)^{th}$ eigenvalue found in Section (4.2). Hence

$$\left[R_y^{-1} \underline{y}\right](t,k) = \sum_{m,n} \frac{y_{mn}}{\rho_{mn}} \psi_{mn}(t,k) \tag{4.49}$$

R_{r_0y} has the $(z', (t,k))^{th}$ entry $E\{r(0,0,z')y(t,k)\}$; so from eq. (4.4)

$$\begin{aligned} R_{r_0y} &= E\{r(0,0,z')y(t,k)\} \\ &= E\{r(0,0,z')\int r(\underline{v})p_k(t+T_k-T(\underline{v},k),(x,y),k)d\underline{v}\} \\ &= \sigma^2 p_k(t+T_k-T((0,0,z'),k),(0,0),k) \end{aligned} \tag{4.50}$$

So we can form the LMMSE beamformed aperture center line by

$$\underline{\hat{r_0}}(z') = \sigma^2 \sum_k \int_{\frac{-\alpha_k T}{2}}^{\frac{\alpha_k T}{2}} p_k(t+T_k-T((0,0,z'),k),(0,0),k) \sum_{m,n} \frac{y_{mn}}{\rho_{mn}} \psi_{mn}(t,k)dt \tag{4.51}$$

4.4 Implementation in MATLAB

In this section we discuss how we implemented the entire scheme in MATLAB. For generating ultrasound RF data we used the well-known Field II simulation program [12] which is based on the calculation of the spatial impulse response.

The first step of the process is the generation of the basis functions using eq. (4.40). For this we have to calculate the eigenfunctions $\nu_{mn}(k)$ of the A_{ij} block of the infinite block matrix $\tilde{A}$ which has the following structure

$$\tilde{A} = \begin{bmatrix} \underline{B}(0) & & & & \\ & \Re\{\underline{B}(\frac{1}{T})\} & -\Im\{\underline{B}(\frac{1}{T})\} & & \\ & \Im\{\underline{B}(\frac{1}{T})\} & \Re\{\underline{B}(\frac{1}{T})\} & & \\ & & & \Re\{\underline{B}(\frac{2}{T})\} & -\Im\{\underline{B}(\frac{2}{T})\} \\ & & & \Im\{\underline{B}(\frac{2}{T})\} & \Re\{\underline{B}(\frac{2}{T})\} \\ & & & & \cdots \quad \cdots \end{bmatrix}$$

The block diagonal entries of $\tilde{A}$ matrix are made of the real and imaginary parts of $\underline{B}$ matrix at frequencies $f_m = \frac{m}{T}$. The entries of the $\underline{B}$ matrix at frequencies $f_m = \frac{m}{T}$ are basically the Fourier series coefficients of $b(t,(k,l))$ at those frequencies.

As $b(t,(k,l)) = \sqrt{\alpha_k \alpha_l} d(t,(k,l))$, we can calculate $b(t,(k,l))$ using the definitions of $d(t,(k,l))$ in eqs. (4.13)-(4.15) and then calculate the Fourier series coefficients at frequencies $f_m = \frac{m}{T}$ to generate the entries of the matrix B.

The time domain expression of $d(t,(k,l))$ involves integration which increases the complexity of computation. To reduce the complexity we used the properties of Fourier transform to get a simplified expression in frequency domain. We can calculate the $(k,l)^{th}$ entries of the $\underline{D}\big(\frac{m}{T}\big)$ matrix using the following expression.

$$D\Big(\frac{m}{T},(k,l)\Big) = \int d(t,(k,l)) \exp\Big(- j2\pi \frac{m}{T} t\Big) dt \tag{4.52}$$

Using the definition of $d(t,(k,l))$ in eqs. (4.13)-(4.15), we get

$$\begin{aligned}
D\Big(\frac{m}{T},(k,l)\Big) &= \int_{\eta_i}\int_{\xi_i}\int_t c\big(t,(\xi_i,\eta_i),(k,l)\big) \exp\Big(- j2\pi \frac{m}{T} t\Big) dt d\xi_i \eta_i \\
&= \int_{\eta_i}\int_{\xi_i}\int_s\int_t q(s,(\xi_i,\eta_i),k) q(s+t,(\xi_i,\eta_i),l) \exp\Big(- j2\pi \frac{mt}{T}\Big) dt ds d\xi_i \eta_i \\
&= \int_{\eta_i}\int_{\xi_i}\int_s q(s,(\xi_i,\eta_i),k) \int_t q(s+t,(\xi_i,\eta_i),l) \exp\Big(- j2\pi \frac{mt}{T}\Big) dt ds d\xi_i d\eta_i \\
&= \int_{\eta_1}\int_{\xi_i} Q\Big(\frac{m}{T},(\xi_i,\eta_i),l\Big) \int_s q(s,(\xi_i,\eta_i),k) \exp\Big(j2\pi \frac{ms}{T}\Big) ds d\xi_i d\eta_i \\
&= \int_{\eta_i}\int_{\xi_i} Q^*\Big(\frac{m}{T},(\xi_i,\eta_i),k\Big) Q\Big(\frac{m}{T},(\xi_i,\eta_i),l\Big) d\xi_i d\eta_i
\end{aligned} \tag{4.53}$$

As $q((\xi_i,\eta_i),t,k) = p((\xi_i,\eta_i),-\alpha_k t,k)$ we get

$$D\Big(\frac{m}{T},(k,l)\Big) = \int_{\eta_i}\int_{\xi_i} \frac{P\big(\frac{m}{T\alpha_k},(\xi_i,\eta_i),k\big)}{\alpha_k} \frac{P^*\big(\frac{m}{T\alpha_l},(\xi_i,\eta_i),l\big)}{\alpha_l} d\xi_i d\eta_i \tag{4.54}$$

So the $(k,l)^{th}$ entry of the $\underline{B}\big(\frac{m}{T}\big)$ matrix is calculated using

$$\begin{aligned}
B\Big(\frac{m}{T},(k,l)\Big) &= \sqrt{\alpha_k \alpha_l} D\Big(\frac{m}{T},(k,l)\Big) \\
&= \int_{\eta_i}\int_{\xi_i} \frac{P\big(\frac{m}{T\alpha_k},(\xi_i,\eta_i),k\big)}{\sqrt{\alpha_k}} \frac{P^*\big(\frac{m}{T\alpha_l},(\xi_i,\eta_i),l\big)}{\sqrt{\alpha_l}} d\xi_i d\eta_i
\end{aligned} \tag{4.55}$$

We calculated the block diagonal entries of the matrix $\tilde{A}$ using the real and imaginary parts of the matrix $\underline{B}\left(\frac{m}{T}\right)$.

In the expression in eq. (4.55), $P\left(\frac{m}{T\alpha_k}, (\xi_i, \eta_i), k\right)$ and $P\left(\frac{m}{T\alpha_l}, (\xi_i, \eta_i), l\right)$ are the scaled Fourier series coefficients for the received signal at the k^{th} and l^{th} element of the aperture for one point scatterer situated at (ξ_i, η_i). To get the $(k, l)^{th}$ entry of the matrix $\underline{B}\left(\frac{m}{T}\right)$ we calculate the product for each point scatterer and then sum them across the region of interest.

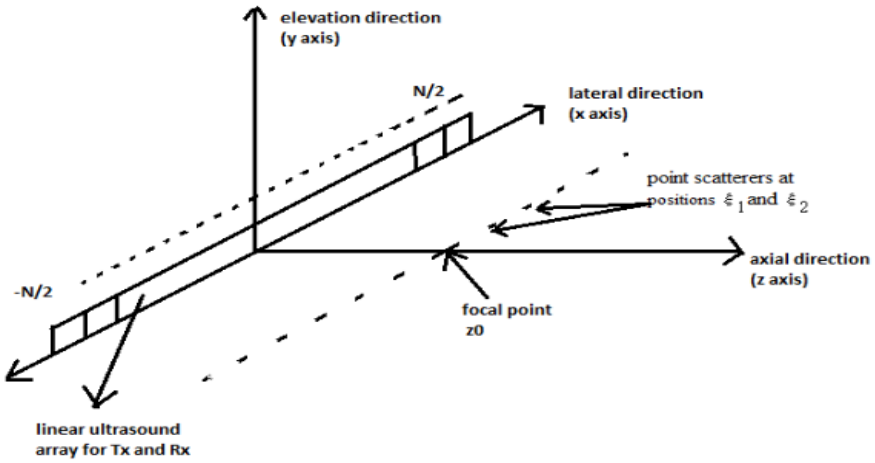

Figure 4.4. Setup for basis generation

We used the setup in Figure 4.4 to generate the basis that consists of a focused linear ultrasound array (for transmission and reception) and a number of point scatterers at the focal point (z_0) of the array separated in the lateral (x) direction.

To calculate the entries of the matrix $\underline{B}$ we calculated the scaling factors α_k's for each element in the aperture and selected a few frequencies $f_m = \frac{m}{T}$ at which we are going to calculate the Fourier coefficients for the center element of the aperture.

For each point scatterer placed at lateral positions ξ_i, where $i = 1, \ldots, n$, we calculated the received signal set $p(t, (\xi_i, \eta_i), k)'$s at each element in the receive aperture and for each frequency f_m and then, we calculated the scaled Fourier coefficients $P\left(\frac{f_m}{\alpha_k}, (\xi_i, \eta_i), k\right)$. We used the MATLAB built-in **fft** function for calculating the

scaled Fourier coefficients. For the k^{th} received aperture signal, we chose a window of length $\alpha_k T$ and calculated a $\alpha_k T$-point FFT on it. Scaling the number of points in the FFT by α_k scaled the frequencies in the spectrum by the factor of $\frac{1}{\alpha_k}$ and gave us the required sequence $P\big(\frac{f_m}{\alpha_k}, (\xi_i, \eta_i), k\big)$. This process is repeated for all the elements in the aperture and the coefficients are stored in a matrix $Q_{\xi_i}\big(\frac{m}{T}\big)$, where ξ_i denotes the lateral position of the point scatterer. The matrix $Q_{\xi_i}\big(\frac{m}{T}\big)$ generated in this way has $(m,k)^{th}$ entries corresponding to the Fourier coefficient calculated at $\frac{f_m}{\alpha_k}$ for the k^{th} aperture element and has the following structure.

$$Q_{\xi_i}\big(\tfrac{m}{T}\big) = \begin{bmatrix} P_{-\frac{N-1}{2}}(0) & \dots & P_0(0) & \dots & P_{\frac{N-1}{2}}(0) \\ P_{-\frac{N-1}{2}}\left(\frac{1}{\alpha_{-\frac{(N-1)}{2}} T}\right) & \dots & P_0\big(\frac{1}{T}\big) & \dots & P_{\frac{N-1}{2}}\left(\frac{1}{\alpha_{\frac{(N-1)}{2}} T}\right) \\ \vdots & & \vdots & \vdots & \vdots \\ P_{-\frac{N-1}{2}}\left(\frac{m}{\alpha_{-\frac{(N-1)}{2}} T}\right) & \dots & P_0\big(\frac{m}{T}\big) & \dots & P_{\frac{N-1}{2}}\left(\frac{m}{\alpha_{\frac{(N-1)}{2}} T}\right) \\ \vdots & & \vdots & \vdots & \vdots \end{bmatrix}$$

The entire process is repeated for all the point scatterers and their corresponding coefficients are stored in individual matrices.

To calculate the $(k,l)^{th}$ entries of $\underline{B}(\frac{m}{T})$ matrix, we calculate the required products $P\big(\frac{f_m}{\alpha_k}, (\xi_i, \eta_i), k\big) P^*\big(\frac{f_m}{\alpha_l}, (\xi_i, \eta_i), l\big)$. For each frequency f_m, we consider the corresponding m^{th} row of the matrices $Q_{\xi_i}\big(\frac{m}{T}\big)$. For each point scatterer, the $(m,k)^{th}$ elements of the matrix $Q_{\xi_i}\big(\frac{m}{T}\big)$ is multiplied by the conjugate of the $(m,l)^{th}$ element of the same matrix. The products generated for all the point scatterers are then summed up to produce the $(k,l)^{th}$ entry of the matrix $\underline{D}(\frac{m}{T})$at that frequency. In our setup, we only considered the point scatterers those are separated in the lateral direction, ignoring the point scatterers in the elevation direction.

The entries of the $\underline{D}(\frac{m}{T})$ matrix are then used to generate the matrix $B = A_p D A_p$, where A_p is a diagonal matrix with diagonal entries $\left\{\frac{1}{\sqrt{\alpha_1}}, \dots, \frac{1}{\sqrt{\alpha_N}}\right\}$. The matrix B is then used to calculate the block diagonal entries of the matrix A. The eigenvectors

of the block diagonal entries A_{ij} are then used to calculate the optimal basis in eq. (4.45).

For a given set of received ultrasound RF signals, at first we generate the Fourier coefficients at scaled frequencies using MATLAB's built-in **fft** for scaled window and **fft** length. The real and imaginary parts of the coefficients are then used to generate y_m using equation (4.40).

For compression we only keep the coefficients that preserve 99.9999% of the total energy and discard the rest of them. For reconstruction, we first use $\hat{Y}_k(\frac{m}{T}) = \sum_n y_{mn}\nu_{mn}(k)$ to generate y_{mn}. These y_{mn}'s are then used to generate the reconstructed signal $\hat{y}_k(t)$ by applying **ifft** at scaled window and FFT length.

For LMMSE estimate calculation, the coefficients y_{mn}'s are divided by the corresponding eigenvalues ρ_{mn} followed by the scaled inverse Fourier transform. The reconstructed signal is then correlated using eq. (4.51) to generate the estimate.

4.5 Experimental Results

We generated a couple of phantom data sets using Field II simulation program to test the performance of our method. The phantoms used different sizes of transducer arrays with different numbers of active elements in the array. We used the data for reconstruction as well as the LMMSE estimate calculation using our approach.

For all the examples, we used 2 cycles of a 3MHz sinusoid pulse for transmission. For the first three cases, the sampling frequency was 100MHz, for the the last example, it was 50MHz. The array of transducers is made of elements which are 5 mm high, 1mm wide and have $\frac{1}{20}$mm distance between them. For the entire process the array was focused at 40mm in the axial direction.

Figure 4.5 and 4.6 show the basis vectors at a frequency at the center of the band for 15 element and 25 element aperture, respectively. The basis function calcula-

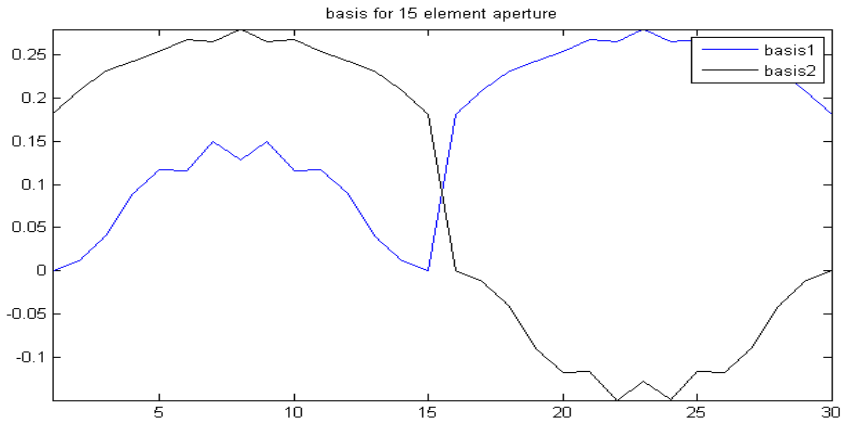

Figure 4.5. First two optimal basis vectors $\nu_{nm}(k)$ for $n = 0, 1; k = 0, \ldots, N-1$ and f_m=3MHz for a 15-element aperture

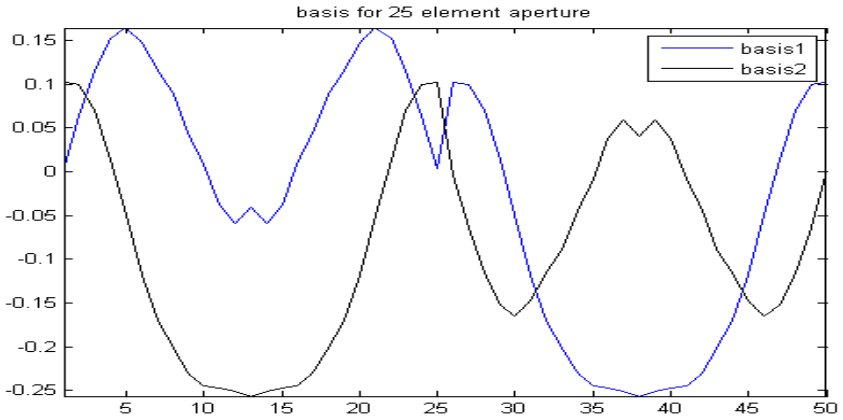

Figure 4.6. First two optimal basis vectors $\nu_{nm}(k)$ for $n = 0, 1; k = 0, \ldots, N-1$ and f_m=3MHz for a 25-element aperture

tion for each frequency showed that only the first 3-5 eigenvectors have significant eigenvalues.

For the first example, we generated a phantom with a 2mm cyst inside that has 2000 point scatterers in it. There are 25 elements in the transmitter and receiver array with 15 active elements for each image line generation. The phantom has a dimension of 7mm×7mm×4mm with starting edge at 39mm. Figure 4.7 shows the actual position of the point scatterers in the phantom in example 1.

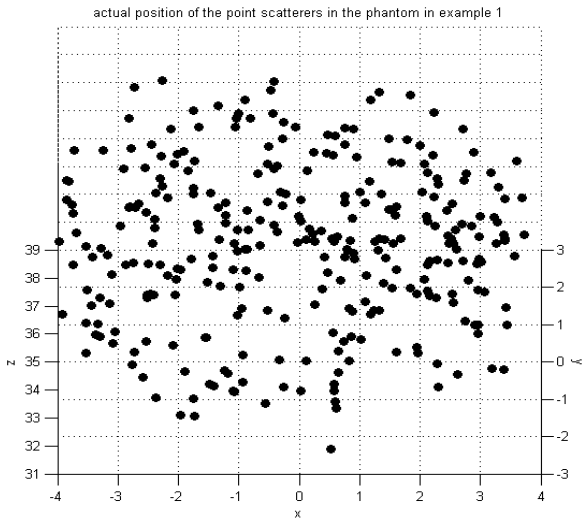

Figure 4.7. Actual position of the point scatterers in the phantom in example 1

Figure 4.8 shows the reconstructed signal using the optimal basis.

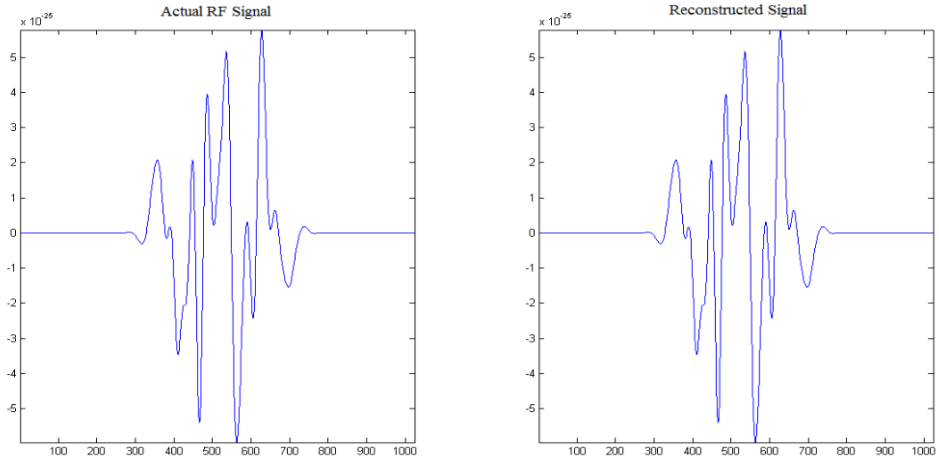

Figure 4.8. Signal reconstruction using optimal basis for 15 element aperture

Figure 4.9 shows the comparison of the delay and sum beamformed image, a reconstruction using the first eigenvector and the LMMSE estimate. The LMMSE estimate has sharper edges in the phantom image.

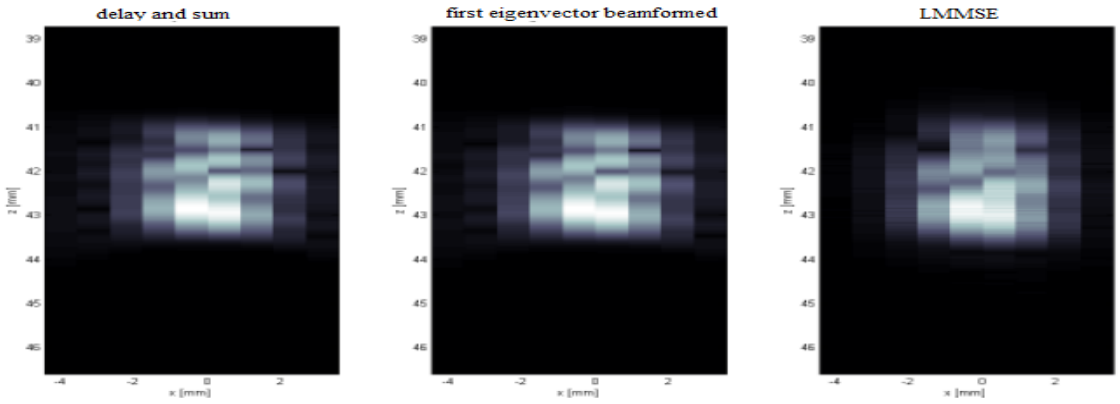

Figure 4.9. Comparison of images generated using different beamforming techniques

Figure 4.10 compares the lateral profile of the cyst in the image and the LMMSE estimate shows the narrower profile, that means the LMMSE estimate concentrates more energy inside the cyst.

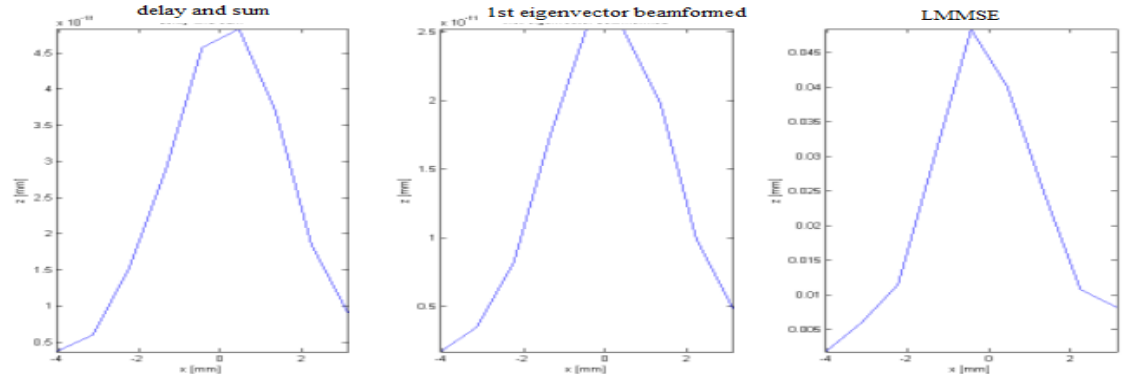

Figure 4.10. Lateral profile of the cyst

For the next example, we worked with a phantom that has 2500 point scatterers and a hollow cyst inside. We used a 45 element transducer array for generating the image where 15 elements are active for generating each image line. The dimension of the phantom are 15mm×5mm×10mm with the starting edge at 30mm. The cyst has 3mm radius and is centered at (0,0,35)mm. The image lines are separated by 0.25mm in the lateral x direction. This setup generates 31 lines in the image. Figure 4.11 shows the actual position of the point scatterers in the phantom in example 2.

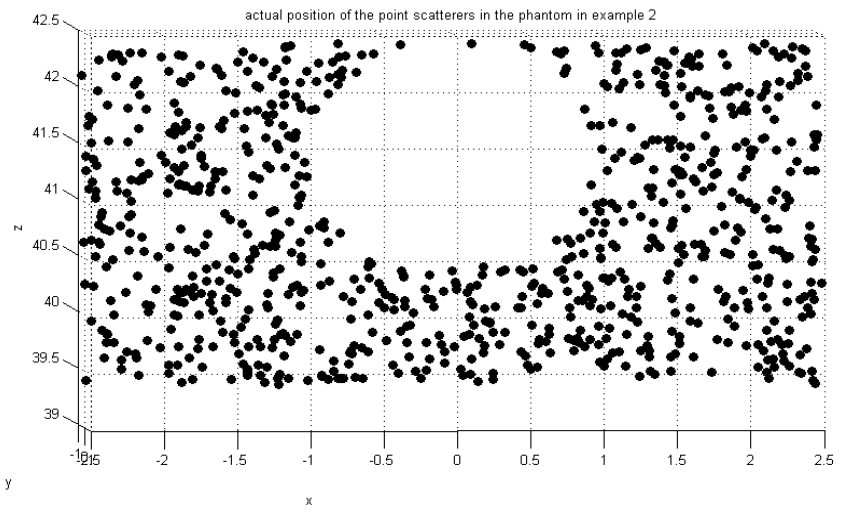

Figure 4.11. Actual position of the point scatterers in the phantom in example 2

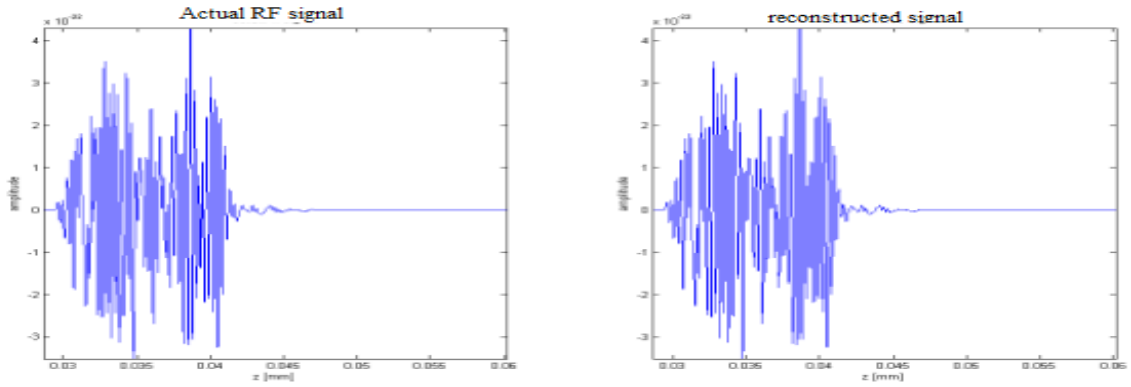

Figure 4.12. Comparison of the actual RF signal and reconstructed signal using optimal basis

Figure 4.12 shows the comparison of the actual signal and the reconstructed signal retaining 99.9999% of the total energy of the received signal. We needed only 6.8682% of the total number of coefficients for this case.

Figure 4.13 shows the comparison of the delay and sum beamformed image, reconstruction using the first eigenvector and the LMMSE estimate.

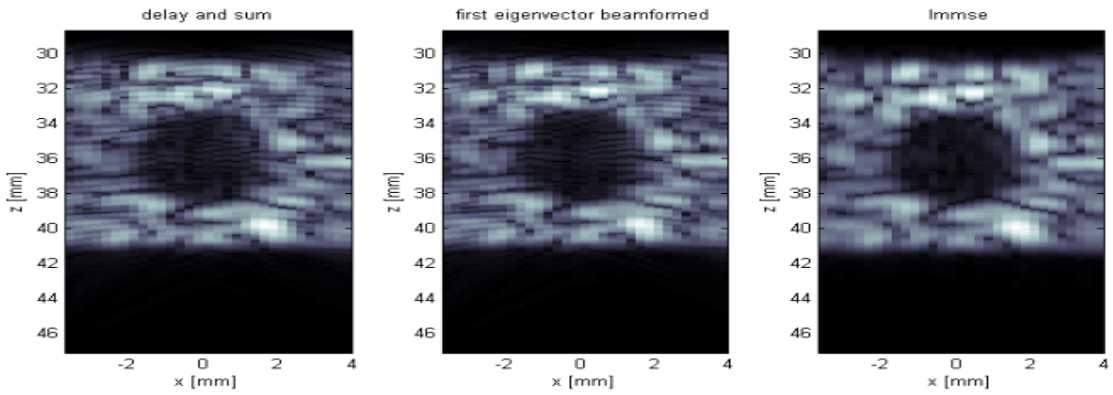

Figure 4.13. Comparison of images generated using different beamforming techniques

In our third example, we used a larger aperture of active elements to generate a phantom that has 2 cysts in it: one with no scatterers inside and another with all the scatterers inside. For this we used a 89 element aperture with 25 active elements during image generation. This setup generates 65 image lines. Figure 4.14 shows the actual position of the point scatterers in the phantom in example 3.

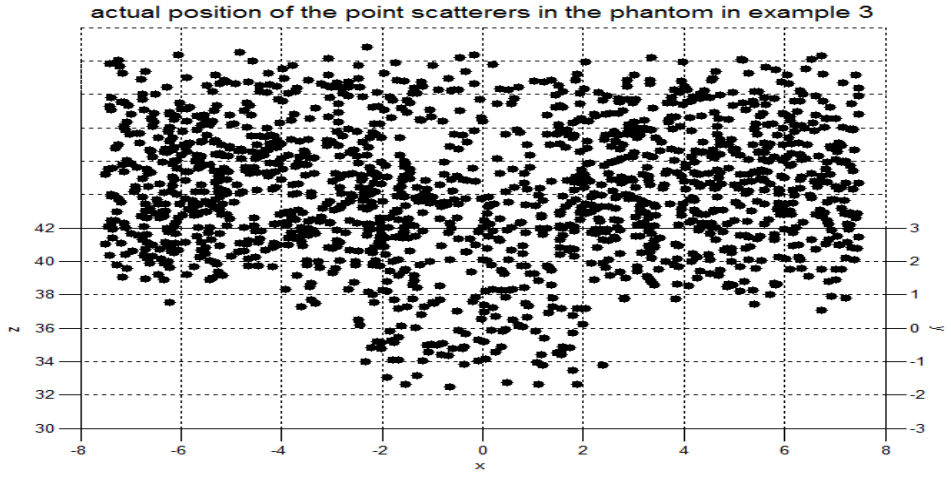

Figure 4.14. Actual position of the point scatterers in the phantom in example 3

Figure 4.15 shows the comparison of the images generated using delay and sum beamformer, beamforming using first eigenvector and also the LMMSE estimate.

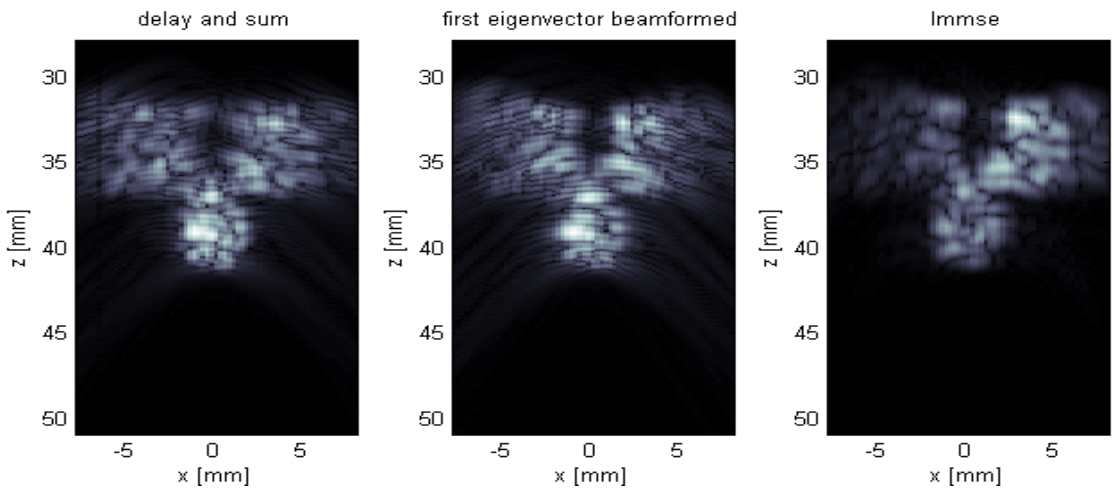

Figure 4.15. Comparison of images generated using different beamforming techniques for a 25 active element transducer array

From the image we can see that the LMMSE estimate shows lesser streaks in the image and shows the patterns in the image more clearly.

For the last example, we used an even larger aperture of 129 elements with 65 active elements in it. We generated a 25mm×2mm×10mm phantom with a 3mm radius cyst inside. There are 2400 point scatterers inside the cyst. This setup generates 64 image lines. Figure 4.16 shows the actual position of the point scatterers in the phantom in example 4.

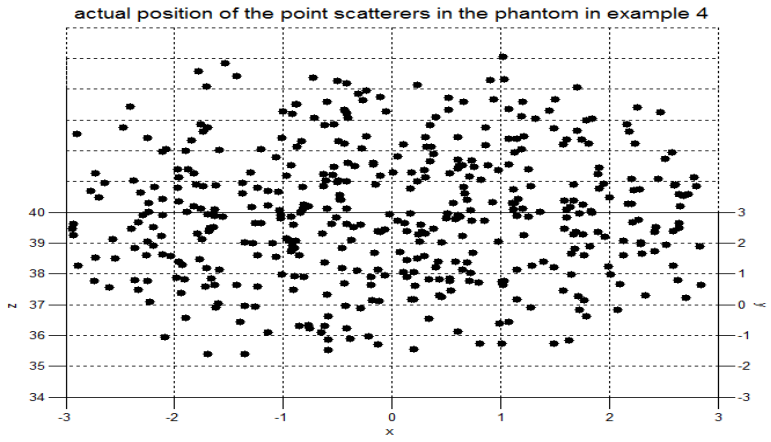

Figure 4.16. Actual position of the point scatterers in the phantom in example 4

Figure 4.17 shows the comparison of images generated using delay and sum and lmmse beamforming and Figure 4.18 shows the lateral profile for the cyst.

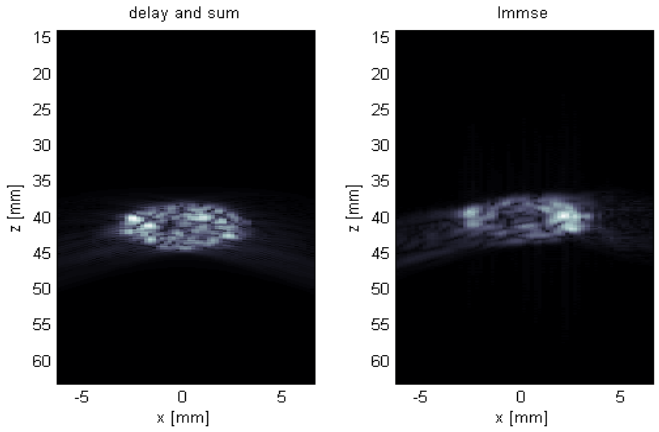

Figure 4.17. Comparison of images generated using different beamforming techniques for a 65 element aperture

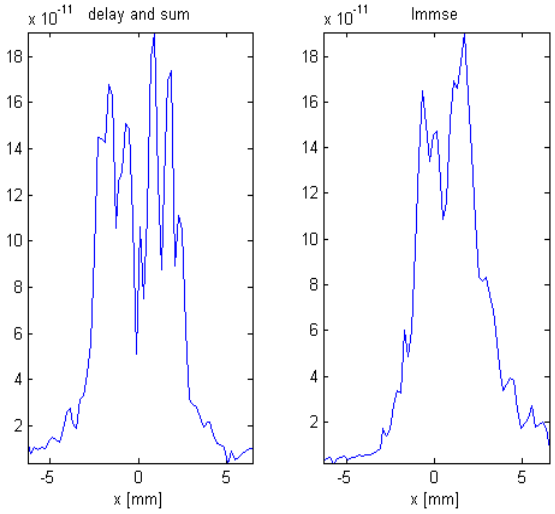

Figure 4.18. Lateral profile of the cyst for a 65 active element transducer array

The following table shows the performance of our compression approach for the 3 examples mentioned above.

Table 4.1. No. of coefficients needed to represent aperture signal sets with MSE=0.0001% using the optimal basis

Criterion	Example 1	Example 2	Example 3	Example 4
No. of Elements in Aperture	15	15	25	65
Window Length (mm)	7.83	31.33	48.59	49.3
No. of Samples at 50 MHz	7626	30516	76880	208000
No. of coefficients used	1382	4252	11946	31916

From the table we can see that the optimal basis gives us a significant amount of compression. For the same level of MSE, using compression in larger windows requires a smaller percentage of coefficients.

For beamforming using the optimal basis coefficients we used eq. (4.51). We used the following values of noise variance σ_N^2 to calculate $\rho_{mn} = \lambda_{mn} + \sigma_N^2$. If $\sigma_N^2 >> \lambda_{mn}$ the beamformed image the effect of noise becomes too dominant. So we had to control the value of σ_N^2 in such a way that the value of σ_N^2 is close to the value of eigenvalues and as the eigenvalues varied from phantom to phantom the value variance varies as well.

Table 4.2. The value of the noise variances used for beamforming using optimal basis

Criterion	Example 1	Example 2	Example 3	Example 4
value of σ_N^2	1e-39	1e-38	1e-38	8e-40

We also compared the compression performances of optimal basis to that of the previous compression approaches we investigated. As the compression we achieved with optimal basis was a 2D compression scheme we compared it with the performance of 2D FFT, 2D wavelet decomposition, 2D wavelet packet decomposition.

Table 4.3-4.5 shows the comparison of the compression performances for example 1. In all the cases we did the compression for 99.99% energy conservation.

Table 4.3. Compression performances of optimal basis and 2D FFT

Criterion	Optimal Basis	2D FFT
% of Energy Conserved	99.99	99.99
% of Coefficients used	6.7847	7.9948
PSNR (dB)	55.5551	55.5511

Table 4.4. Compression performances of different wavelets for 2D wavelet decomposition

Criterion	db10	coif5	sym6	sym8
% of Energy Conserved	99.99	99.99	99.99	99.99
% of Coefficients used	13.7493	13.3485	13.7699	13.8679
PSNR (dB)	55.5308	55.5355	55.5469	55.5612

Table 4.5. Compression performances of different wavelets for 2D wavelet packet decomposition

Criterion	db10	coif5	sym6	sym8
% of Energy Conserved	99.99	99.99	99.99	99.99
% of Coefficients used	8.0175	7.092	9.9867	8.7411
PSNR (dB)	55.5524	55.5662	55.5474	55.5219

From the tables we can see that optimal basis performance is better than all the other 2D compression approaches for the same level of MSE.

4.6 Comparison with the 2D FFT

In our preliminary investigations, the 2D FFT showed pretty good compression results. So we decided to check how much improvement we get over the 2D FFT by using our approach. For this we took the data for the 15 element aperture in example 2 and compared the performance of both approaches.

From table 4.3 and 4.6 we can see that our approach has a slightly better performance than the 2D FFT. For same amount of energy in the reconstructed signal we needed almost 1118 coefficients less than that used for 2D FFT. In other words,

Table 4.6. Comparison with the 2D FFT

Criterion	Our Approach	2D FFT
% of Energy Conserved	99.9999	99.9999
% of coefficients used	6.5290	7.4449
No. of coefficients used	7970	9088

the 2D FFT required approximately 1.14× the number of coefficients of the optimal basis to achieve the same MSE.

For further comparison of the performance of the two approaches we performed LMMSE beamforming using both the optimal basis coefficients and the 2D FFT coefficients and compared the final images.

We used eq. (4.51) for calculating the LMMSE beamformed aperture center line except for this case we used the 2D FFT coefficients as y_{mn} rather than the optimal coefficients. For this we need to calculate the eigenvalues ρ_{mn} of the 2D FFT basis. In the derivation we defined $b(t,(k,l)) = \sqrt{\alpha_k \alpha_l} d(t,(k,l))$. For the 2D FFT case we assume $\sqrt{\alpha_k \alpha_l} = 1$ and then $\tilde{b}(t,l) = b(t,(0,l)) = d(t,(k,l))$ will be the stationary autocorrelation at the center of the aperture. Then the 2D FFT of $\tilde{b}(t,l)$ will give us the eigenvalues ρ_{mn}. $R_y^{-1}y$ in eq. (4.51) can be calculated by

$$\begin{aligned} R_y^{-1}y &= \sum_{m,n} \frac{y_{mn}}{\rho_{mn}} \psi_{mn}(t,k) \\ &= \text{ifft}\left\{ \frac{Y(k_1,k_2)}{\tilde{B}(k_1,k_2) + \sigma_N^2} \right\} \end{aligned} \tag{4.56}$$

$Y(k_1,k_2)$ are the 2D FFT coefficients of the aperture signal set. The ifft part in the equation comes from the fact that in this case $\psi_{mn}(t,k)$ are the 2D FFT basis. The LMMSE at the center of the aperture can be calculated using

$$\tilde{r}_0 = R_{r_0 y} R_y^{-1} y$$
$$= \sigma^2 \sum_k \int_{-\frac{\alpha_k T}{2}}^{\frac{\alpha_k T}{2}} p_k(t + T_k - T((0,0,z),k),(0,0),k)) \text{ifft}\left\{ \frac{Y(k_1,k_2)}{\tilde{B}(k_1,k_2) + \sigma_N^2} \right\} dt \tag{4.57}$$

Figure 4.19, 4.20, 4.21 and 4.22 show the comparison of the images generated by LMMSE beamforming using optimal basis and 2D FFT coefficients for example 1, example 2, example 3 and example 4 respectively. The images show that the images generated using 2D FFT coefficients have slight streaks and are slightly blurrier than the optimal basis coefficients generated image. Still the 2D FFT approximations are pretty close to the optimal one. The reason behind the similarity between the images comes from the fact that we are using actual pulses generated in MATLAB to correlate both the coefficients. We used the same value of σ_N^2 for the LMMSE using optimal basis and 2D FFT coefficients.

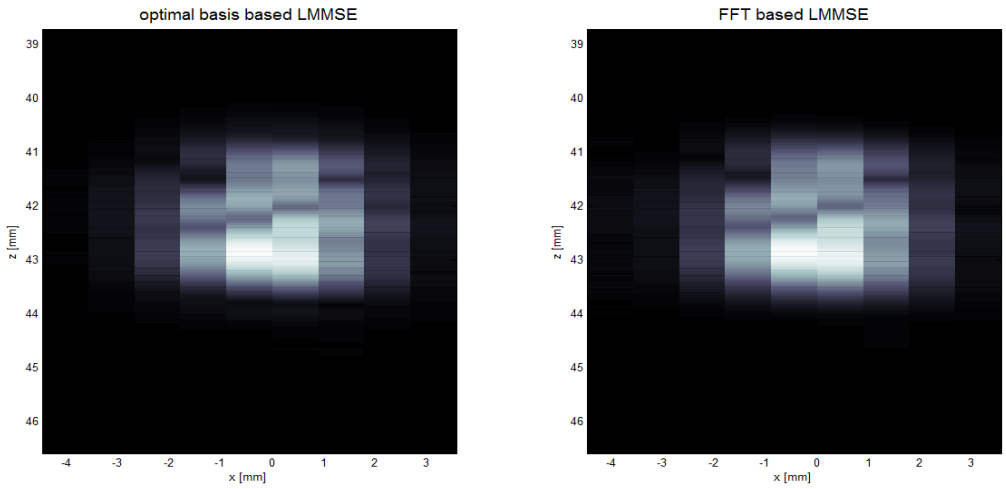

Figure 4.19. Comparison of the beamformed images using optimal basis coefficients and 2D FFT coefficients for example 1

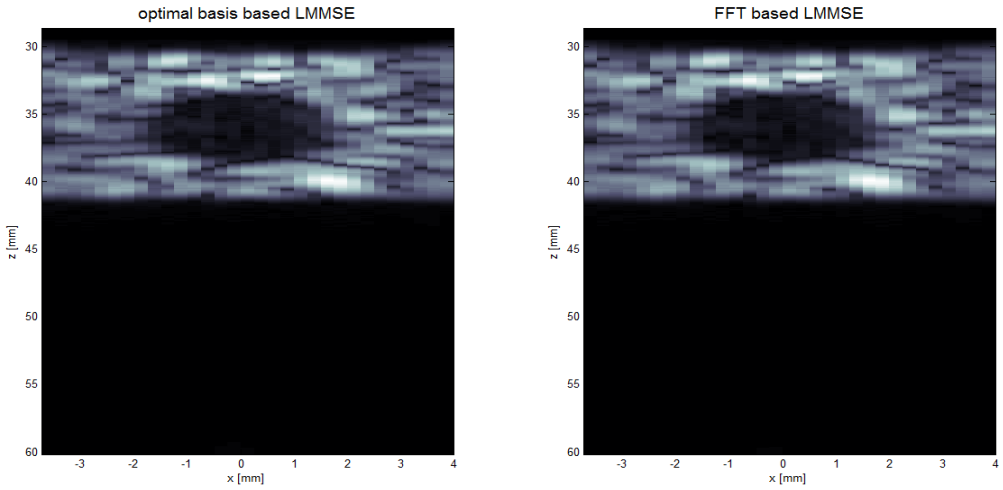

Figure 4.20. Comparison of the beamformed images using optimal basis coefficients and 2D FFT coefficients for example 2

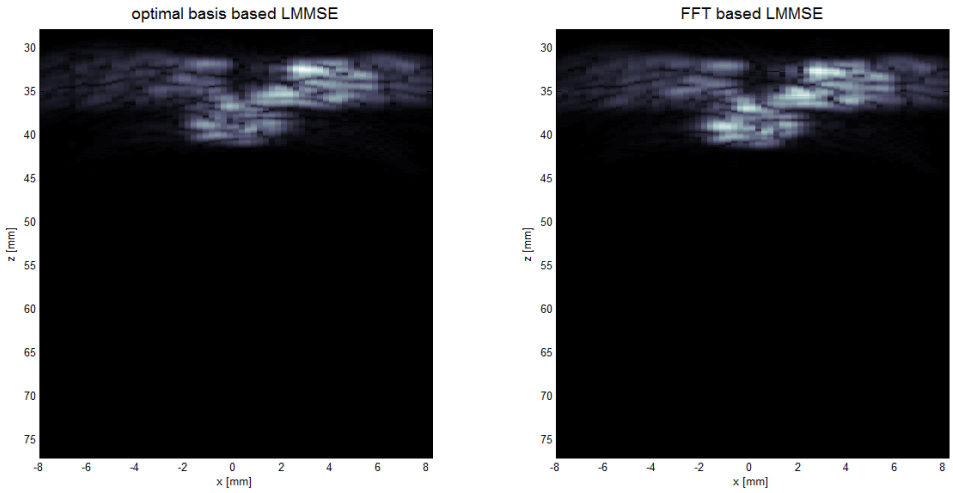

Figure 4.21. Comparison of the beamformed images using optimal basis coefficients and 2D FFT coefficients for example 3

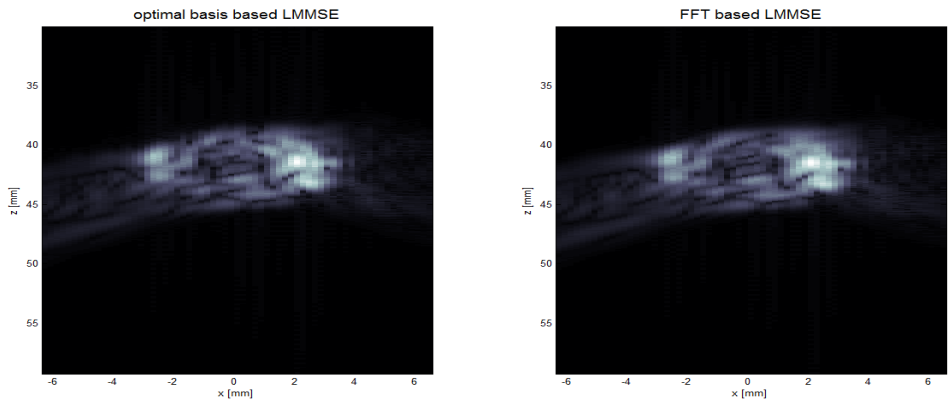

Figure 4.22. Comparison of the beamformed images using optimal basis coefficients and 2D FFT coefficients for example 4

Finally, we compared the block diagrams of the approaches to see which approach is more feasible to implement.

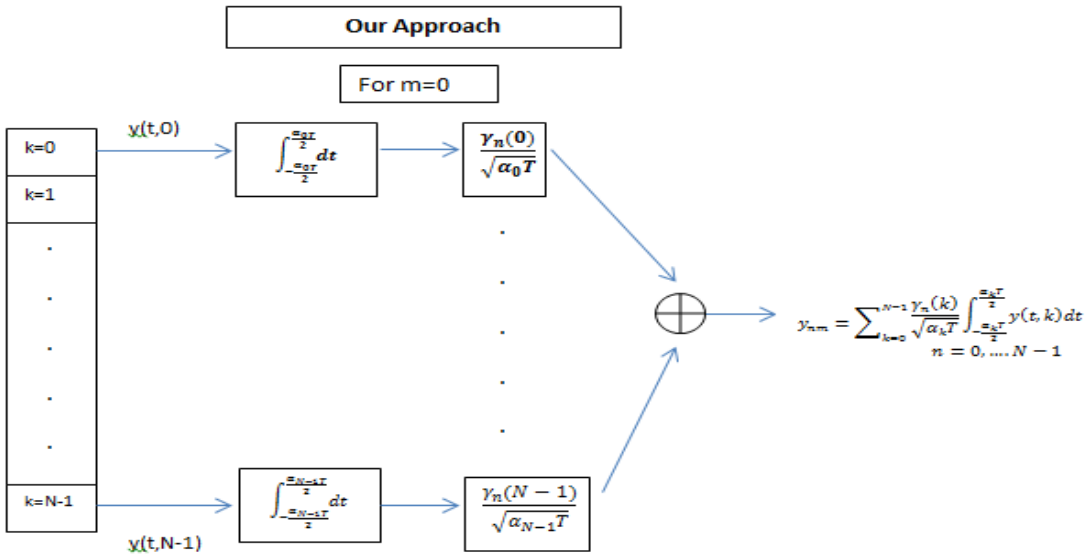

Figure 4.23. Block diagram for the implementation of optimal basis approach for $m = 0$

Figure 4.23 and 4.24 shows the block diagram for optimal basis approach for $m = 0$ and $m = 1, 2, \ldots$ respectively. From Figure 4.24 we can see that if we use the optimal basis we can implement the axial scaled Fourier series part easily in analog domain. For the spatial processing, we need to use weights determined by eigenvectors of the block diagonal entries of the A matrix, as described in section 4.2.

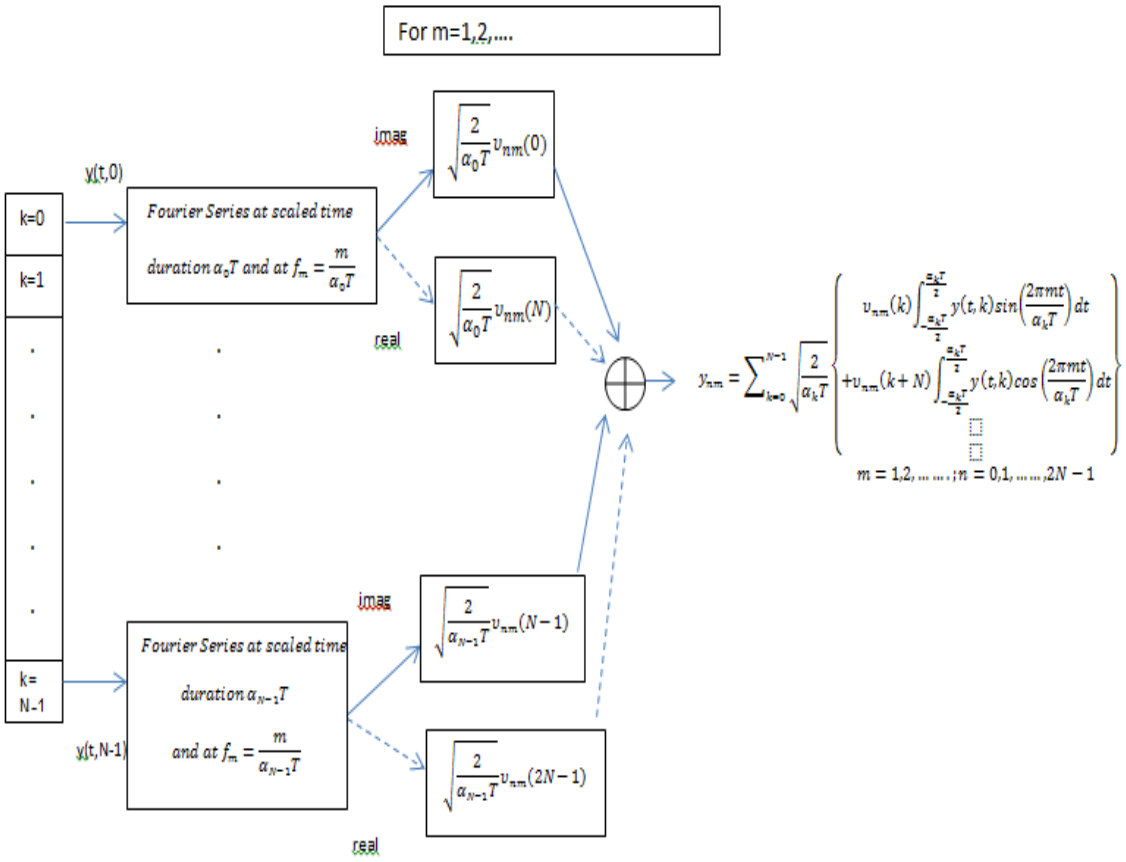

Figure 4.24. Block diagram for the implementation of optimal basis approach for $m = 1, 2, \ldots$

Figure 4.25 shows the implementation of the 2D FFT in block diagram. The 2D FFT can be implemented in two different ways- by doing the axial Fourier series followed by spatial DFT or doing the spatial Fourier series at first followed by the axial Fourier Series. Figure 4.25 shows two different ways of implementing 2D FFT.

The axial Fourier series part in the first approach can be done in real-time but the spatial DFT part needs to be done in digital domain. But in the second approach we can do the spatial Fourier series first by calculating a weighted sum in real time. Then the weighted sums go through a real time Fourier series as well.

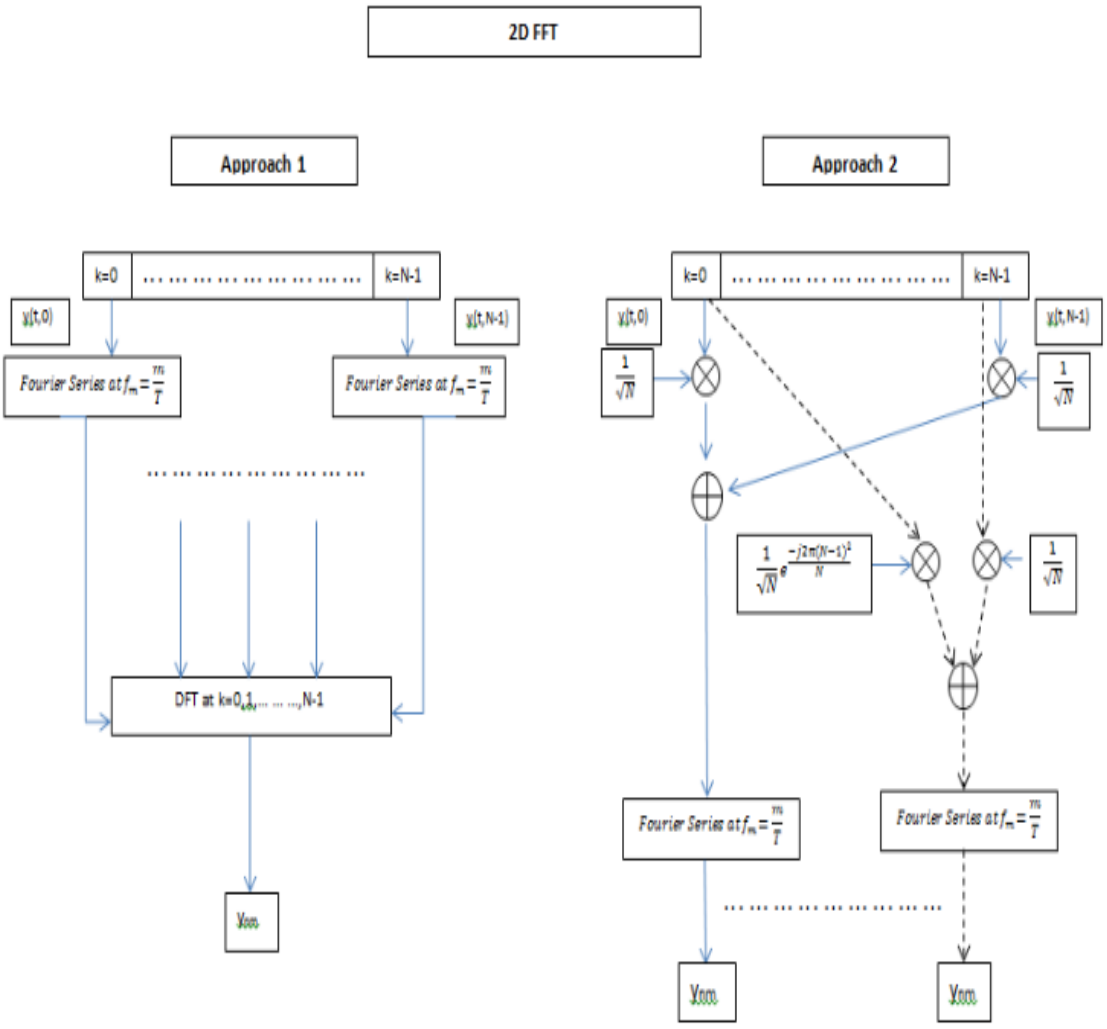

Figure 4.25. Block diagram for implementation of 2D FFT in two different ways

As our intention was to implement a feasible compression scheme in real-time it now becomes a matter of trade off between the two schemes. We can compress a given signal set entirely in real-time (approach 2 in 2D FFT) but in that case we would have to give up a certain amount of compression. On the other hand implementing the

optimal compression provides great compression but at the cost of implementing the spatial part in the digital domain. In the end it is the ultrasound system designer's decision of how much compression he is willing to achieve at the desired cost of implementation.

CHAPTER 5

CONCLUSION

The goal of this work was to find an optimal compression scheme for ultrasound RF signals. For this at first we gave some idea about the compression problem that motivated us and also the part of the ultrasound system we are working with. Then we investigated the performance of existing works in signal compression as well as ultrasound signal compression. Finally we derived a basis in the form of eigenfunctions of the autocorrelation function of the received signal set. The coefficients of the signal set with respect to the basis are computed by taking Fourier Transforms (at frequencies scaled by element position) in time, followed by weighted linear combinations of the real and imaginary parts of the Fourier transform across the aperture at each frequency. Tests on simulated data sets generated with the Field II simulation program showed that the optimal basis required about 14% fewer coefficients than the 2D FFT to achieve a mean-squared error of 0.0001%. The optimal basis was also used to formulate a LMMSE beamformed aperture center line which was then compared to standard delay-and-sum beamformed aperture center line. The LMMSE results generally showed less smearing and streaking of image features.

We also briefly discussed how compression with both the optimal basis and 2D FFT can be implemented. Finally, we compared the performances of beamforming using optimal basis and 2D FFT coefficients.

Our work on optimal basis can be expanded to 2D array case. Future work can also include actual implementation of the approach in circuit.

BIBLIOGRAPHY

[1] Abbey, C. K., Nguyen, N. Q., and Insana, M. F. Optimal Beamforming in Ultrasound using the Ideal Observer. *IEEE Transactions on Ultrasonics, Ferroelectrics and Frequency Control 57*, 8 (August 2010), 1782–1796.

[2] Ali, M., Magee, D., and Dasgupta, U. *Signal Processing Overview of Ultrasound Systems for Medical Imaging*, November 2008. Texas Instruments White Paper.

[3] Friboulet, D., Liebgott, H., and Prost, R. Compressive Sensing for Raw RF Signals Reconstruction in Ultrasound. *2010 IEEE International Ultrasonics Symposium Proceedings* (2010), 367–370.

[4] Jensen, J. A. A Model for the Propagation and Scattering of Ultrasound in Tissue. *J. Acoustical Society of America 89*, 1 (January 1991).

[5] Jensen, J. A. Simulation of Advanced Ultrasound Systems using Field II. *IEEE International Symposium on Biomedical Imaging: Nano to Macro 57*, 8 (2004), 636–639.

[6] Khare, K. Bandpass Sampling and Bandpass Analogues of Prolate Spheroidal Functions. *Signal Processing 86* (2006), 1550–1558.

[7] Mansour, M., and Ali, M. Lossless Compression of Ultrasound RF Data. *2010 IEEE International Ultrasonics Symposium Proceedings* (2010), 2282–2285.

[8] Mansour, M., and Ali, M. Lossless Compression of Ultrasound RF Data. *2010 IEEE International Ultrasonics Symposium Proceedings* (2010), 2299–2302.

[9] Senaya, S., Chaparro, L. F., Zhao, R., Sclabassi, R. J., and Sun, M. Discrete Prolate Spheroidal Sequences for Compressive Sensing of EEG Signals. *SIAM Review 25*, 3 (July 1983), 379–393.

[10] Shlens, J. *A Tutorial on Principal Component Analysis*, April 2009.

[11] Slepian, D. Some Comments on Fourier Analysis, Uncertainty and Modeling. *SIAM Review 25*, 3 (July 1983), 379–393.

[12] Srinath, M. D., Rajasekaran, P. K., and Viswanathan, R. *Introduction to Statistical Signal Processing with Applications*. Prentice Hall Information and System Series, 1996.

[13] Tur, R., and Eldar, Y. C. Innovation Rate Sampling of Sampling of Pulse Streams with Application to Ultrasound Imaging. *IEEE Transactions on Signal Processing 59*, 4 (2010), 1827–1842.

[14] Wang, P., Shen, Y., and Wang, Q. Gaussian Wavelet Based Dynamic Filtering (GWDF) Method for Medical Ultrasound Systems. *Ultrasonics 46* (2007), 168–176.

[15] Zemp, R. J., Abbey, C. K., and Insana, M. F. Linear System Models for Ultrasonic Imaging: Application to Signal Statistics. *IEEE Transactions on Ultrasonics, Ferroelectrics and Frequency Control 50*, 6 (June 2003), 642–654.